A review of recent developments in schlieren and shadowgraph techniques

Topical Review

A review of recent developments in schlieren and shadowgraph techniques

Gary S Settles[1,3] and Michael J Hargather[2]

[1] FloViz Inc., Port Matilda, PA 16870, United States of America
[2] Mechanical Engineering Department, New Mexico Tech, Socorro NM 87801, United States of America

E-mail: drgaryssettles@gmail.com and michael.hargather@nmt.edu

CrossMark

Abstract

Schlieren and shadowgraph techniques are used around the world for imaging and measuring phenomena in transparent media. These optical methods originated long ago in parallel with telescopes and microscopes, and although it might seem that little new could be expected of them on the timescale of 15 years, in fact several important things have happened that are reviewed here. The digital revolution has had a transformative effect, replacing clumsy photographic film methods with excellent—though expensive—high-speed video cameras, making digital correlation and processing of shadow and schlieren images routine, and providing an entirely-new synthetic schlieren technique that has attracted a lot of attention: background-oriented schlieren or BOS. Several aspects of modern schlieren and shadowgraphy depend upon laptop-scale computer processing of images using an image-capable language such as MATLAB™. BOS, shock-wave tracking, schlieren velocimetry, synthetic streak-schlieren, and straightforward quantitative density measurements in 2D flows are all recent developments empowered by this digital and computational capability.

Keywords: schlieren, shadowgraph, high-speed imaging, digital image processing, MATLAB, flow visualization, background-oriented schlieren

(Some figures may appear in colour only in the online journal)
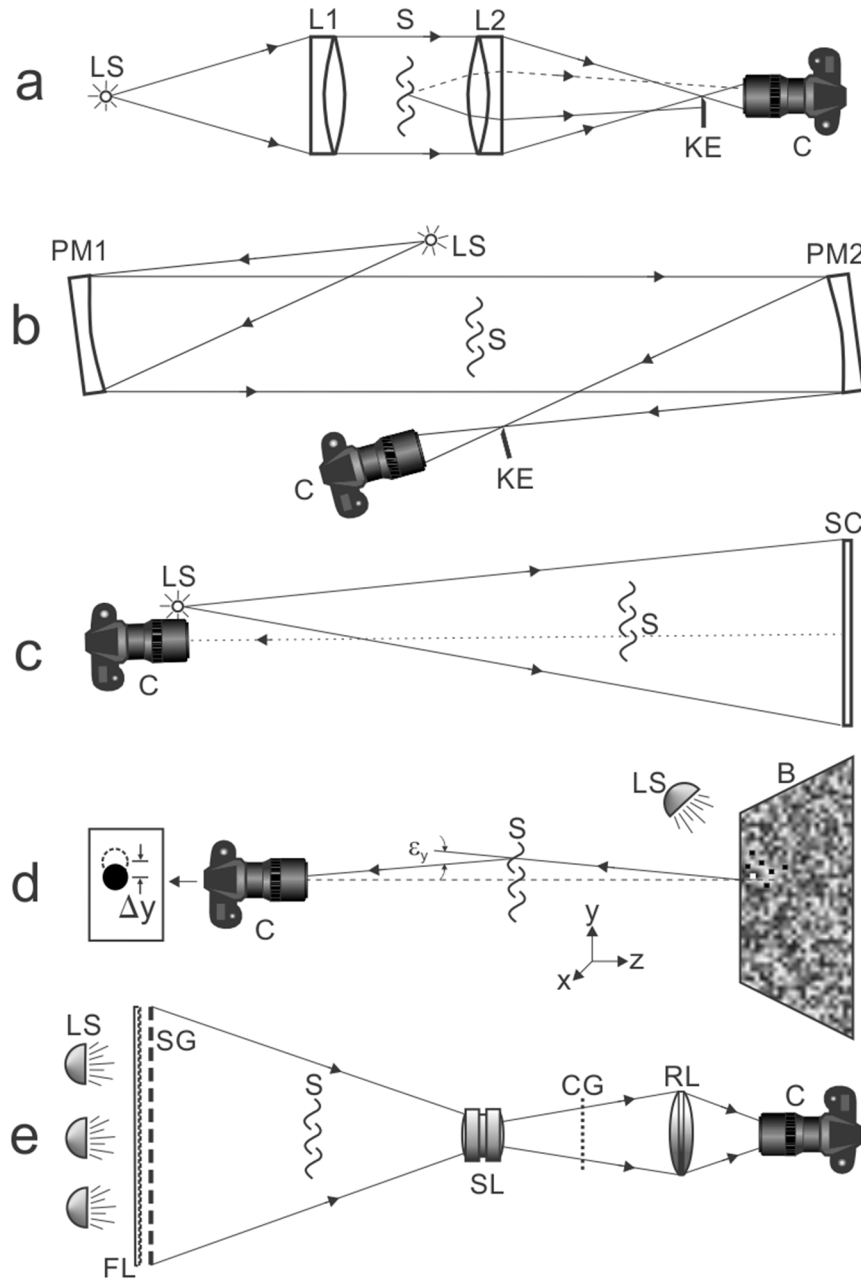
1. Introduction

Schlieren and shadowgraphy were formally originated by Robert Hooke in the 17th century, well before their time [1]. Upon reinvention by August Toepler in the mid-19th century, schlieren optics (named for streaks or striae) became a standard laboratory tool that played a key role in observing shock waves, to name just one important discovery. Though simpler than schlieren, shadowgraphy came along a bit later. Together, these optical tools for seeing the invisible had a great influence upon wind-tunnel testing and the development of high-speed aircraft in the mid-20th century. Today their use is widespread across scientific experimentation. Generally using non-coherent 'white' light for imaging, schlieren and shadowgraphy are very visual and were once thought to be mere qualitative visualization methods lacking the quantitative power of laser interferometry, but that is shown no longer to be true in this review.

The present objective is to review significant advances in schlieren and shadowgraph techniques in the 15 years since [1], especially the influence of digital imaging and image processing. The expected audience includes current and prospective users of these instruments in fluid dynamics and heat transfer research, as well as in many other disciplines. Although the construction and setup of schlieren and shadowgraph equipment remains primarily do-it-yourself, a description is provided of the few commercial instruments that are currently available.

Schlieren and shadowgraphy are optical techniques that rely upon precise lenses, mirrors, and cameras to image refractive

[3] Author to whom any correspondence should be addressed.

Figure 1. Diagrams of five types of schlieren and shadowgraph instruments discussed in this paper: (a) Toepler's lens-type schlieren system, (b) z-type schlieren system using twin parabolic mirrors, (c) direct shadowgraphy, (d) background-oriented schlieren (BOS), (e) focusing (lens-and-grid) schlieren system.

disturbances in transparent media. Detailed descriptions of the various optical arrangements, along with the supporting theory, are found in [1] and many other references cited therein. Here, for brevity, five simplified optical systems are diagramed in figure 1.

Figure 1(a) shows a classical schlieren setup first used by Toepler [2]. Light from a small bright source LS is collimated by lens *L*1 and brought to a focus by lens *L*2, beyond which the light beam is captured by a camera *C*. A sharp knife-edge KE is inserted at the focus, blocking part of the light. A refractive disturbance in the air between the two lenses, labeled *S* for *Schlieren*, is represented by squiggles. In this simple diagram a light ray refracted upward (dashed line) avoids

the knife-edge and proceeds to the camera, while another refracted downward (solid line) is blocked by the knife-edge. Generalizing this to every ray in the light beam, we have an instrument that captures a pure phase disturbance *S* as a grayscale amplitude image in the camera. This is the essence of what schlieren instruments do. Readers familiar with Fourier optics [3] will also recognize figure 1(a) as a Fourier optical processor, the knife-edge acting as a half-plane mask of the spatial frequency spectrum.

The lens diameter in figure 1(a) determines the field-of-view of the instrument. For diameters greater than 15 cm or so, parabolic telescope mirrors PM1 and PM2 are used instead, figure 1(b), thus folding the optical path and introducing

usually-manageable off-axis aberrations. These mirrors range from a few cm up to more than 1 m in diameter, and they represent by far the most common class of traditional schlieren instruments. A simple and effective single-mirror, double-pass instrument is also useful [1], but is not shown here.

Note that the schlieren arrangements in figures 1(a) and (b) can also produce shadowgrams upon removal of the knife-edge and defocusing the camera lens. (Shadowgraphy cannot occur when the optics are sharply focused on the schlieren object [1].)

Turning to figure 1(c), a very simple and robust optical arrangement called direct shadowgraphy requires only a small bright light source LS (typically 1 mm or less in diameter), a camera *C*, and a projection screen SC. Light refraction by *S* casts, upon the distant screen, a telling shadow of itself that we call a *shadowgram*. More detail on this is found later in section 9 on retroreflective shadowgraphy.

Next comes a new synthetic schlieren technique, background-oriented schlieren or BOS, figure 1(d). As in shadowgraphy, a camera images a distant screen, but in this case the screen is a patterned background. Images of schlieren object *S* in front of this background show subtle shifts due to refraction when compared with an undistorted 'tare' background image. Digital image processing is able to measure these shifts and construct from them a pseudo-schlieren image without the usual optics of figures 1(a) and (b). This background-distortion effect was known to schlieren pioneer H Schardin 80 years ago [4], but modern digital computers and cameras were necessary to make it a useful schlieren technique, discussed in detail in section 4.

Finally, figure 1(e) diagrams a 'lens-and-grid' or 'focusing' schlieren system of the type proposed by Weinstein [5]. In this case the effective light source is a large source grid SG, backlit by several lamps whose light is directed by a Fresnel lens FL toward a 'schlieren lens' SL, which can be a large-format camera lens (a large, precise, expensive lens used in studio photography). This lens produces a reduced image of the source grid that is partially blocked by a matching negative cutoff grid CG. A relay lens RL then conveys the schlieren beam to camera *C*. This arrangement has a narrow depth of focus at *S*, which is useful in avoiding the usual schlieren-optics trait of integrating everything along its optical path into a single 2D image. A recent improvement involving projecting the source grid is covered in section 10.

The theory that supports schlieren and shadowgraphy, based mostly on geometrical optics with additional consideration of diffraction effects, can be found in [1, 4, 6] and other background sources. The Gladstone–Dale law, for example, is the simple relation between the density ρ of a fluid and its refractive index *n*,

$$n - 1 = k\rho \tag{1}$$

where *k* is a constant for a given fluid. However, the light-and-dark patterns seen in a schlieren image do not directly indicate *n*, but rather its gradients $\partial n/\partial x$ and $\partial n/\partial y$ perpendicular to both the optical axis and the knife-edge orientation. In shadowgrams it is the 2nd spatial derivative (Laplacian) that is displayed.

Against that background, this review considers how new cameras, light sources and laptop-scale computer image processing have recently changed schlieren and shadowgraphy. It begins with the shift from photographic film to digital imaging.

2. Digital versus analog imaging

A great deal has been said about the transition from photographic film to digital imaging. Konica-Minolta stopped making their respected line of film cameras in 2006 and Kodak itself went bankrupt in 2012. Now digital cellphone cameras allow everyone to be a photographer, with results published immediately on social media. Some worry that the nuance of film has been lost [7] while others ask how many image megapixels are enough. All the darkrooms are now gone, replaced by image-processing software that makes it too easy, some believe, to alter the evidence.

For scientific imaging, though, and especially for schlieren and shadowgraphy, there is a strong case in favor of the digital revolution and little reason to mourn the demise of film.

2.1. Digital high-speed video cameras

Traditional film-based high-speed drum, rotating-mirror, rotating-prism, and streak cameras have largely been rendered obsolete by a new generation of easy-to-use digital high-speed cameras with CMOS sensors, megapixel resolution up to 20 000 frames s^{-1} (fps), and peak frame rates extending to one million fps and beyond. Commercial examples of such cameras include the Photron Fastcam SA-Z (photron.com) and the Vision Research Phantom V2512 (phantomhighspeed.com).

Triggering these cameras for events like shock tube tests, gunshots and explosions is greatly simplified by a rolling memory buffer that continuously records several real-time seconds of data until the user stops recording. By stopping upon hearing the 'bang,' the images of a test will always be found within the final second of data and hard-wired triggering complications are avoided. Unlike their predecessors, these cameras make the results available immediately after the test.

Recent high-speed cameras by Shimadzu and Kirana can reach frame rates of 5–10 million fps, but they only provide 100 or a few hundred frames. In this case a hard-wired trigger is needed in order to capture a brief event.

Undeniably these new digital cameras are expensive, costing in the range of $20 000–$200 000US. They can alternatively be rented for short periods at reasonable expense.

Strong illumination is needed for some experiments that image large objects with μs exposures. Traditional schlieren optics, however, project a light beam directly onto the camera sensor, which usually provides enough illumination for most purposes. A retroreflective shadowgraph setup that requires a powerful arc lamp for high-speed video recording is described in section 9.

The ease-of-use of the new high-speed video cameras is unprecedented compared to the old photographic technology. It permits experiments that were once too time-consuming and

costly to be practical. Deriving quantitative data from high-speed video records is also now straightforward, as described in several later sections. Overall, these cameras open a new vista (paraphrasing Robert Hooke [8]) for schlieren and shadowgraphy to peer into the workshop of nature.

Interested readers should also see the related reviews by Versluis [9] on high-speed imaging in fluids and Kleine *et al* [10, 11] on time-resolved visualization of compressible flows.

2.2. Digital single-lens-reflex (DSLR) cameras

At the beginning of the 21st century, traditional consumer-grade 35 mm single-lens-reflex film cameras (SLRs) were widely used for schlieren and shadowgraph imaging. Their advantages included reasonable pricing, a wide range of interchangeable lenses, and a large lens aperture that avoided vignetting the schlieren beam on its way to the camera's film plane. Video cameras were also available that recorded on magnetic tape in the PAL or VHS formats at 25 or 30 fps.

Now these cameras are relics, replaced by digital SLR cameras (DSLRs) yielding images of high-enough megapixel resolution to produce acceptable magazine-cover images in full color, as well as high-definition (HD) video. In the laboratory they outperform their film predecessors in almost every way.

Schlieren images often do not meter for exposure in the same way as traditional photographs, which once resulted in 1 or 2 stops of incorrect schlieren film exposure. Now a few digital test shots, with results seen immediately on a screen at the back of the camera, are sufficient to establish the correct exposure. The emulsion speed and color balance once required different film types, but these factors are now adjustable over wide ranges by digital camera settings. The DSLR camera should be put on fully-manual setting with the aperture wide open to avoid vignetting the image when used with the schlieren instruments shown in figures 1(a), (b) and (e). Without variable aperture, exposure control still remains manageable by shutter speed, ISO speed, external ND filters, or by varying the intensity of the schlieren light source. For direct shadowgraphy and BOS (figures 1(c) and (d)) vignetting is not an issue, and a small lens aperture insures that the screen or background is in sharp focus.

There is a wide range of interchangeable lenses for DSLRs, although schlieren imaging often requires up to a 300 mm zoom lens to fill the image plane with a mirror or a test object that is relatively distant. Outboard focusing lenses were once common between knife-edge and camera, but nowadays a camera lens can usually be found that works without them.

In 2008 Nikon introduced its model D90 DSLR, with a 12.3 megapixel sensor that produced both still images and 720p HD video at 24 fps. Since then every new DSLR on the market has included a video capability. Current top-of-the-line DSLRs from Nikon and Canon have up to 36-megapixel sensors and record 1080p HD video. This is important for schlieren and shadowgraphy because the video is shot through the same large-aperture lens as are the still images. Most digital camcorders and all cellphone cameras are without

interchangeable lenses and have apertures that are hopelessly small for traditional schlieren imaging using the instruments of figures 1(a) and (b).

One DSLR problem still remains: although they have built-in shutter speeds as short as 125 μs, their CMOS rolling-shutter sensors do not respond well to 1 μs-range pulsed exposures in open-shutter mode. Scientific cameras are available with global shutters to handle such short exposures. Other than that, the modern DSLR camera is fully functional for schlieren and shadowgraph still-imaging and HD video at standard speed, it is affordable, and it also has the resolution needed for BOS imaging.

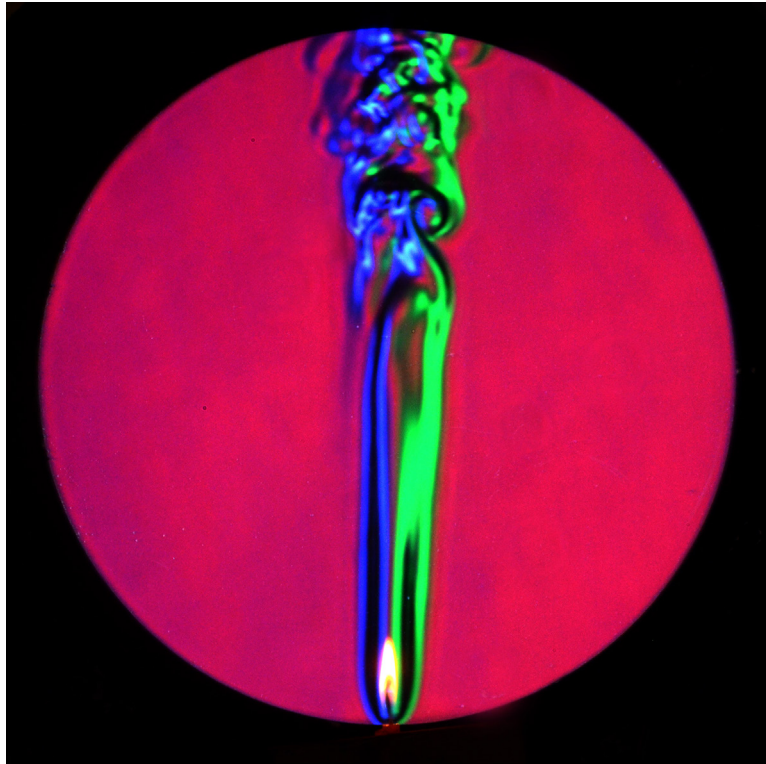### 2.3. What did we lose with the demise of photographic film?

Without film, the time-honored Cranz–Schardin camera [12] is now replaced by the digital high-speed cameras described above. Polaroid roll-and sheet-film packs, once used for fool-proof high-speed exposure tests, are now gone. Optical systems requiring sheet-film cutoffs, such as the focusing schlieren systems exemplified by figure 1(e), are in jeopardy, but see section 10 for a digital replacement. Color-transparency cut-offs for rainbow schlieren imaging [13] can still be shot on 35 mm Fujifilm, although commercial film processing may be hard to find. An alternative is an online digital-image-to-film service such as that provided by gammatech.com.

3. The rise of the LED as a scientific light source

In the second half of the 20th century, light sources for schlieren and shadowgraphy comprised an assortment of spark gaps, lasers, laser-induced breakdown sources, xenon tubes, arc lamps, and incandescent-filament lamps [1]. During this period the light emitting diode (LED) was under development and saw commercial use only in panel indicator lamps. Since around 2000, however, advanced LEDs have made great strides in domestic illumination, automotive lamps, etc, and have not been overlooked in scientific illumination [14–16]. For schlieren and shadowgraphy, the LED is poised to become the ideal non-coherent light source.

The ubiquitous, inexpensive 5 mm T-1¾ LEDs, for example, typically have 1 mm diameter emitters. This is small enough to produce sharp shadowgrams, but not too small to be an effective schlieren lamp. A variety of wavelengths is available for special purposes, but one gets the best resolution from a non-coherent phosphor-conversion 'white-light' LED (actually slightly bluish). As an example, the superbrightleds.com RL5-W18015 Cool White LED consumes 0.11 W and projects a 15° beam through a clear lens with 18 candela luminous intensity. It makes an excellent compact general-purpose schlieren and shadowgraph light source, runs on batteries for hours, and costs only $1US.

In selecting from the broad array of T-1¾ LEDs, one has the choice of diameter, emission wavelength, luminous intensity, and beam viewing angle. For shadowgraphy it is the emitter diameter that counts, and should be chosen in the range of 1 mm or less. Schlieren instruments such as those

Figure 2. Example color schlieren image of a candle plume captured using an adjustable-slit cutoff and a 3-emitter tricolor LED as a light source.

of figures 1(a) and (b) are best illuminated by the narrowest-viewing-angle LEDs available, ideally matching the *f*/numbers of typical schlieren lenses and mirrors. Otherwise choose the highest luminous intensity available; too bright is not usually a problem, but too dim is.

In an effort to produce a tunable white light source, some LEDs are made with separate red, green and blue emitters. Such is the superbrightleds.com Tricolor RL5-RGB-C, which has 472 nm (blue), 630 nm (red), and 525 nm (green) emitters in a linear array. This LED delivers 5 candela luminous intensity in a 15° beam through a clear lens, and currently costs $1.59US. It can be repurposed as a color schlieren light source by using an adjustable slit as a cutoff in schlieren instruments like those diagramed in figures 1(a) and (b). The slit is adjusted to block most of the blue and green light, but to allow all of the red light from the central LED emitter to go through to the camera. The result is a very saturated color schlieren image in green and blue against a red background. Since each emitter is powered through its own anode in a common-cathode arrangement, the power level of the red emitter can be scaled back in order to mute the red background for best results. An example LED color schlieren image of a candle plume is shown in figure 2.

These small LEDs produce plenty of light for ordinary schlieren imaging, but for high-speed video or retroreflective shadowgraphy (section 9) more power is required. LEDs up to the 30 W range are currently available, though with much larger emitters. Depending upon emitter size and shape, an LED can sometimes be used directly at the focus of the first schlieren lens or mirror, thus eliminating the usual condenser and slit [1, 17] or allowing the slit to be combined with the LED source in close contact. Further, linear chips-on-board

LEDs such as those made by Vollong Electronics could be arranged to make a self-illuminated, continuous or pulsed source grid for a focusing schlieren system of the type shown in figure 1(e).

But the best thing about LEDs for schlieren and shadowgraphy is their well-behaved ability to pulse repeatedly down to the 100 ns range [9, 17–19], which they do better and cheaper than any of the other available light sources. Spark sources [1, 20], considering their cost, high-voltage hazard and poor repeatability, are made obsolete by the LED. Likewise xenon discharge-tube sources [1, 19] are more expensive than LEDs and have a long pulse 'tail' [19, 21] that confuses particle image velocimetry (PIV) and schlieren velocimetry alike (section 6).

Willert and colleagues took the unusual step of including both a circuit diagram and a parts list for their pulsed-LED source [17]. They overdrove the LED with a 200 A current in short pulses until it approached failure in order to extract the maximum light output. A subsequent do-it-yourself pulsed LED source with some improvements upon Willert's original costs only $125US to build [19].

The high-power LEDs used in [17–19] are typified by the green Luminus (luminus.com) CBT-120, which has a 2.6×4.6 mm emitter and puts out 800–2100 lumens. The emitter is too large for shadowgraphy but is suitable for schlieren [18]. Such LEDs are typically used for projection displays. It is very likely that more powerful, higher-current examples will become available in the future. Not knowing the nature of these makes it difficult to give specific selection advice. However, a curious fact from Willert *et al* [17] is that the thickness of the LED bonding wires matters, since these can melt at high pulse currents and cause failure.

Commercial high-speed LED light sources are also available from light-speed-tech.com, psp-tsp.com, flovizinc.com and hardsoft.kki.pl. The same LED source provides both continuous-wave illumination for alignment and observation and pulsed output for high-speed imaging. For PIV and schlieren velocimetry, it is double-pulsed with a pulse width sufficient to freeze the motion and a variable pulse separation that depends upon the speed of the flow under study. Not long ago only lasers could do this, and at much greater cost.

Among lasers, compact arc lamps and LEDs as schlieren light sources, the latter have the least eye safety hazard potential. Some compact arc lamps pose a UV radiation hazard, and of course laser beams can focus upon the retina and damage it but spatially-noncoherent LED emissions pose much less risk.

4. Background-oriented schlieren (BOS), aka synthetic schlieren

Background-oriented schlieren is unquestionably the most significant recent development in this field. Invented almost simultaneously in England and Germany [22, 23] just before the turn of the century, BOS has generated a flurry of interest in schlieren imaging similar to that of the early days of high-speed wind tunnel testing. A recent survey of the topic by Raffel [24] cited 115 references, and the numbers continue to grow. A selection of recommended BOS reading is given here in [24–37].

The British BOS inventors saw, using a setup related to figure 1(e), the opportunity to replace the troublesome cutoff grid computationally [22]. Without it, the equipment was no longer schlieren optics but the computer nonetheless produced a pseudo-schlieren image which they named *synthetic schlieren*. The German group instead approached the problem from a PIV background, noting that optical distortion of a PIV-like speckled image produced a second image that could be digitally processed, along with the first, to yield pseudo-particle displacements characterizing the distortion field: *background-oriented schlieren*. Either way, this new approach demands modern computerized optical processing and digital imaging. It is actually synthetic background-distortion schlieren, but the BOS acronym has taken a firm hold.

Here only a brief description and a list of the advantages and disadvantages of BOS as a new schlieren method are presented. Then BOS backgrounds, cameras, and processing software are considered, followed by several examples. Much is necessarily omitted, but we have tried to provide the reader with comprehensive references.

Returning to figure 1(d), the image of a spot on the background B, seen along the dashed straight line without schlieren S in place, is shifted (solid line) by the refraction of S. This shift is seen, by way of the small refraction angle ε_y, as a displacement Δy of the spot on the camera image sensor. Δy can be measured by comparing background images with and without S using digital image cross-correlation software that detects the shift within a small interrogation window. Once Δy is known, the refraction angle ε_y is quickly found from the trigonometry of the setup. But ε_y is the result of

a line integral of the refractive-index gradient $\partial n / \partial y$ along the optical axis z through schlieren object S according to schlieren theory [1, 35],

$$\varepsilon_y = \frac{1}{n} \int \frac{\partial n}{\partial y} \mathrm{d}z = \frac{Z}{n_\infty} \frac{\partial n}{\partial y} \tag{2}$$

and this is the same ε_y that generates the grayscale pattern of a schlieren image in the traditional instruments shown in figures 1(a) and (b). Once we have ε_y and ε_x in a 2D matrix, assigning grayscale values yields a pseudo-schlieren image that is, for practical purposes, the real thing.

For a planar 2D schlieren object of length Z along the optical path, the refractive index gradient can be assumed to be constant along the optical axis and the integral can be simplified. This is indicated in equation (2), where the ambient-air refractive index is given as n_∞. Axisymmetric schlieren objects require a more-sophisticated Abel-transform treatment, e.g. [21]. Multiple views and a tomographic reconstruction must be performed for fully-3D flows [24].
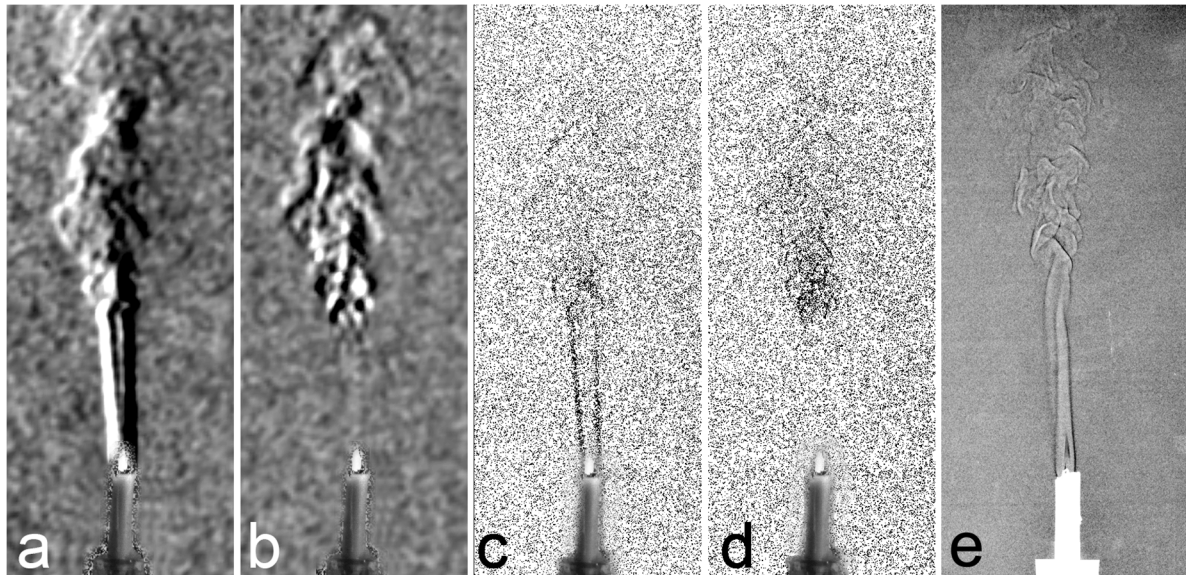
4.1. The advantages of BOS

4.1.1. Schlieren imaging without large, expensive, precision optics. Or, as inventor Meier put it [28], BOS has 'extremely modest technical requirements.' With this comes the advantage of portability and the use of existing and natural backgrounds to be discussed later.
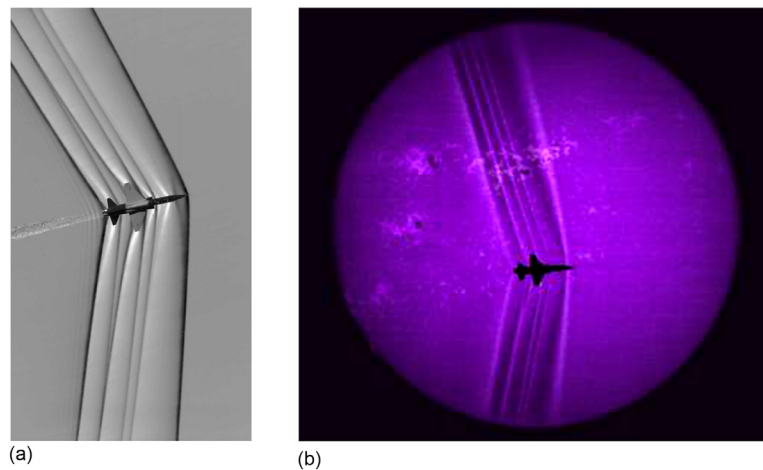
As an example, a simple BOS setup according to figure 1(d) was used to photograph the plume of a candle, figure 3(a). The Photron Mini UX100 camera was 2.4 m from the candle, which was 0.6 m from the background. Figure 3(a) was produced from the digital correlation of a lit-candle image and a tare image using commercial software. The effective field-of-view is about 0.5 m high, or twice that of the mirror-type schlieren system used in figure 2, yet the overall lengths of the two optical systems are about the same. A setup according to figure 1(b) with two precise 0.5 m parabolic mirrors could produce a sharper, less-noisy schlieren image with the same field-of-view as figure 3(a), but at orders of magnitude greater equipment cost. (Figures 3(b)–(e) are reserved for later discussion.)

4.1.2. Very large fields of view. Unlike the traditional schlieren optics of figures 1(a) and (b), but as in direct shadowgraphy and lens-and-grid schlieren (figures 1(c) and (e)), the BOS field-of-view can be at least half as large as its background. When vast natural backgrounds are used, the field-of-view becomes truly impressive; big enough, for example, to observe full-scale helicopters and supersonic aircraft in flight, figure 4 and [38–41].

4.1.3. Unique solutions to some problems. These include the large fields-of-view just described, as applied to aircraft and to outdoor explosions [42–44], and schlieren imaging inside the test sections of large wind tunnels [41, 45, 46]. For example, slotted or perforated transonic test sections, which can be as large as 5 m across, generally have no significant optical access for traditional schlieren or shadowgraphy. In

Figure 3. BOS candle plume (a) image correlation, lit candle and tare image, (b) image correlation, two lit-candle images 0.1 s apart, (c) subtraction of tare image from lit-candle image, (d) subtraction of two images 0.1 s apart, (e) tone-inverted shadowgram shown for comparison.

Figure 4. (a) NASA AirBOS image of a transonic T-38 aircraft taken from another aircraft using the desert floor as background. Reproduced from NASA (www.nasa.gov/centers/armstrong/features/shock_and_awesome.html). See also [38]. The image has been corrected and processed from original BOS data. (b) NASA BOSCO (CaKeBOS) image of T-38 aircraft seen against the disc of the sun by a telescope with a calcium K-line filter. Reproduced from NASA (www.nasa.gov/feature/ground-based-schlieren-technique-looks-to-the-sun-and-moon). See also [39].

such cases the BOS camera can peer through a tiny access port at a background pattern applied to the opposite wind-tunnel wall, thus imaging at least a part of a refractive flowfield that cannot otherwise be observed.

4.2. The disadvantages of BOS

4.2.1. Limited resolution. Because image cross-correlation algorithms average over their interrogation window size, BOS always delivers less image resolution than comparable traditional schlieren instruments [24]. Likewise an increase in BOS sensitivity requires a larger interrogation window, and thus delivers lower resolution [30]. The resolution loss is most noticeable at

discrete flow features such as shock waves. The same issue is experienced in PIV and in solid-mechanics displacement and strain measurements by digital image correlation.

4.2.2. Limited real-time imaging. While traditional schlieren and shadowgraphy offer a ready live image, BOS requires post-processing in order to see anything. A capable laptop computer running an FFT-based image cross-correlation code typically needs 30 s or more to process a megapixel-range image pair. Even at a reduced frame rate, it generally takes time to make a BOS video this way (see an online example by LaVision [47]). The computer power and graphics processing unit needed to do this in real time is not currently available for

BOS, except for the simple background-subtraction approach described below. Improvements in BOS processing algorithms and speed could come from parallel work now going on in PIV processing.

The British inventors of BOS recognized at the outset the need for a qualitative BOS mode yielding a live flow visualization in addition to quantitative off-line BOS processing [22, 25]. By subtracting the no-flow 'tare' image pixel values from those of a current BOS video frame, squaring or taking the absolute value, scaling the result for contrast, and displaying it as the current output frame, one gets a real-time 'poor-man's BOS' visualization of a flow (figure 3(c)). Compared to a full image cross-correlation, figure 3(a), this operation is simple and fast enough to run, for example, as an interpreted MATLAB™ script without much or any frame delay. Though not an impressive visualization, image subtraction is a solution to BOS's live imaging problem that has caught on [34, 48–50]. An online video example by FloViz Inc. is given in [51]).

As an interesting historical sidelight, live qualitative BOS video was up and running for internal gravity wave visualization in the Geophysical and Environmental Fluid Dynamics Summer Schools at Cambridge University beginning in 1991, 7 years before it was first publicly presented [52].

4.2.3. Difficulty in attaining sharp focus on both subject and background. Referring again to figure 1(d), it is clear that the BOS background *B* must be in sharp focus on the camera sensor [24], but what about the schlieren object *S* under study? Theoretically the depth-of-field of the camera can extend to include both, but this may result in the distance from camera to *S* becoming impractically large, especially in a laboratory where dimensions are constrained. Inevitably some blurring of *S* creeps into most BOS experiments. This violates a principle of schlieren imaging (but not shadowgraphy) dating back to Toepler, that the subject of study should always be in sharp focus [1].

Meier [28] recommends a small camera aperture and a short distance from *S* to *B* in order to minimize this problem, although the latter also reduces the BOS sensitivity. Raffel [24] recommends that the dimension of the image blur should remain considerably smaller than the interrogation window size during BOS processing. Ultimately it is up to the investigator to not accept blurry, out-of-focus BOS imaging. If the BOS camera has a sufficient depth-of-field, the background *B* should be at the far end and the schlieren object *S* at the near end of it, rather than centering the depth-of-field on the background. Further discussion of this issue is found in [37].

4.2.4. Non-parallel illumination. BOS shares with direct shadowgraphy and lens-and-grid schlieren the issue of having a small camera lens looking at a large background grid along non-parallel rays. This complicates the quantitative measurement of schlieren object *S* and even the geometrical treatment of any 3D object centered in the *S* plane. Avoiding these pitfalls is an important reason for the expensive lenses and mirrors in traditional parallel-light schlieren instruments. One can partially mitigate the problem by making the axial length of a BOS system very long compared to the background

size, which is usually impractical, or by using a large lens or parabolic mirror to accept only parallel light from the background (telecentric mode), which defeats the chief advantage of BOS. Overall, this drawback is a reminder that, while Δx and Δy are measured quantitatively, there can still be issues that invalidate BOS for quantitative flow measurements.

4.2.5. Vibration sensitivity. BOS compares a flow-on image with a no-flow tare image acquired earlier. Vibration, or anything other than the schlieren object *S* that changes between these two exposures, is a problem [30]. In particular, Elsinga *et al* [29] issue the following warning: 'Problems related to unsteady displacement of the tunnel and vibration are intrinsic to the supersonic wind tunnel environment.' The problem of background motion was likewise intrinsic to the flight-test experiments performed in [38], where an image registration algorithm was implemented to realign the high-speed image sequence of the aircraft to the tare background image before performing the BOS processing that resulted in figure 4(a).

For turbulent flows, abandoning the tare image and instead processing two flow-on images separated by a short time interval (but not so short as to 'freeze' the turbulence) provides a BOS image solely of turbulent flow structures. This was suggested by Meier [28] and was carried out by Hargather and Settles [53]. The difference in the appearance of the BOS result as a function of these two processing approaches is shown in figures 3(a) and (b), where the same image of a candle plume is compared to a tare background image before the candle is lit (figure 3(a)) and to another lit-candle-plume image recorded 0.1 s after the first (figure 3(b)). Figure 3(a) is a traditional BOS image of the candle plume including laminar-to-turbulent transition. Figure 3(b), however, is actually a *temporal* BOS image showing only regions where the refractive-index field has changed between exposures, and thus revealing the turbulence but not the laminar plume. This temporal BOS processing method can be valuable, but should not be used for quantitative measurements because the absolute refraction angle is not known, only the relative angle from one turbulent image to the next.

4.3. BOS backgrounds

Like grids for computational fluid dynamics (CFD), BOS backgrounds have almost become their own independent topic of study. In the beginning, the British group used regular horizontal-line grids while the Germans used random, PIV-like dot screens. More than 15 years later the latter approach has taken precedence, because any regular background pattern is susceptible to aliasing during the processing of BOS images [54].

Procedures and codes to generate backgrounds have been proposed, though none seem to be available for public use. The idea is simple enough, though, requiring only a about a dozen lines of MATLAB™ code: A 2D matrix of any desired size is created and filled with random numbers using the `rand` function, then binarized using `im2bw`. The matrix can be printed as an image with a fine-scale random pattern, or with a little more effort random spot structures of various sizes can

be built up and printed. References [30] and [53] discuss BOS background design in more detail, and Goldhahn and Seume [32] suggest a somewhat-different procedure.

Experience reveals that it is not the actual size of the background dots that matters, but rather the number of pixels each covers when focused upon the camera image sensor. Raffel [24] recommends background spots of 3–5 pixel size as a reasonable compromise, though 2–3 pixels gives better sensitivity if attainable. Defining background dots this way requires prior knowledge of the dimensions of the BOS layout and the camera-lens characteristics. Practically, a variety of backgrounds with different-sized spots is called for. These are inexpensive and useful to have on hand.

Very large backgrounds could be made by silk-screening random-dot patterns on cloth. Postersmith.com, for example, accepts a PDF image file and prints it on fabric panels 1.2×1.8 m in size. Black sequin fabric material (e.g. from backdropexpress.com) could provide a BOS background of bright dots on a black ground if appropriately lighted. Outdoors, certain decorative concrete-block and stucco walls can provide large random BOS backgrounds when sunlit at an oblique angle.

Atcheson *et al* [33] advocate the use of a single wavelet-noise background with a range of different feature scales as an alternative to having a collection of different random-dot backgrounds. This approach did not respond well to blur produced by the schlieren object, however, in trials carried out by Vinnichenko *et al* [54].

Vinnichenko *et al* [54] considered the optimal BOS background question and concluded in favor of the 2–3 pixel randomly-distributed dot size mentioned above. Good dot contrast is important to the image correlation, but there is limited incentive to construct backgrounds more complicated than random dot patterns. Placing these dots on retroreflective sheet material has some advantage of gain in situations where lighting the background is hampered, as in large wind-tunnel investigations [46].

Colored backgrounds (CBOS) are used [24, 36] to take advantage of the RGB sensors inherent in modern megapixel-range digital color cameras. As many as 8 different color channels can be extracted from CBOS images, which are then useful to manage distortion and blur caused by schlieren phenomena having strong gradients, especially shock waves.

Natural backgrounds hold a special appeal to those who see BOS as an opportunity to get out of the laboratory. It was a dream of Schardin [4] and others to learn how to see refractive phenomena on a grand scale, but this first needed portable computer muscle and computer vision to evolve, and film to step aside. Before the turn of the century [1], outdoor schlieren was limited to strong disturbances (shock waves, jet exhausts, and fires) seen against the horizon or the sun.

Meier emphasized the importance of large natural backgrounds in his original BOS patent application [23], but no natural background performs quite as well as the correct random-dot screen, and not every outdoor scene is able to serve. Several efforts [31, 34, 55, 56] have tried to characterize and classify the suitability of natural backgrounds.

Continuous-gradient backgrounds, displayed on a computer monitor, have recently been suggested to eliminate the need of an image correlation for BOS processing [57]. This technique uses a known spatial variation of pixel intensities in the BOS background that is recorded with a pre-test image. Subsequent images of the schlieren object in front of the background provide a distortion of the gradient pattern, which can be analyzed on a pixel-by-pixel basis using simple subtraction of image intensities to determine a local 'pixel shift' in the gradient direction, and thus the local refraction angle.

Finally, note the use of laser speckle [50, 58] as a BOS background for better sensitivity, short *S*-to-*B* distances, and sharp focus on *S* rather than on the background. Reference [59] is cited as background reading on this topic.
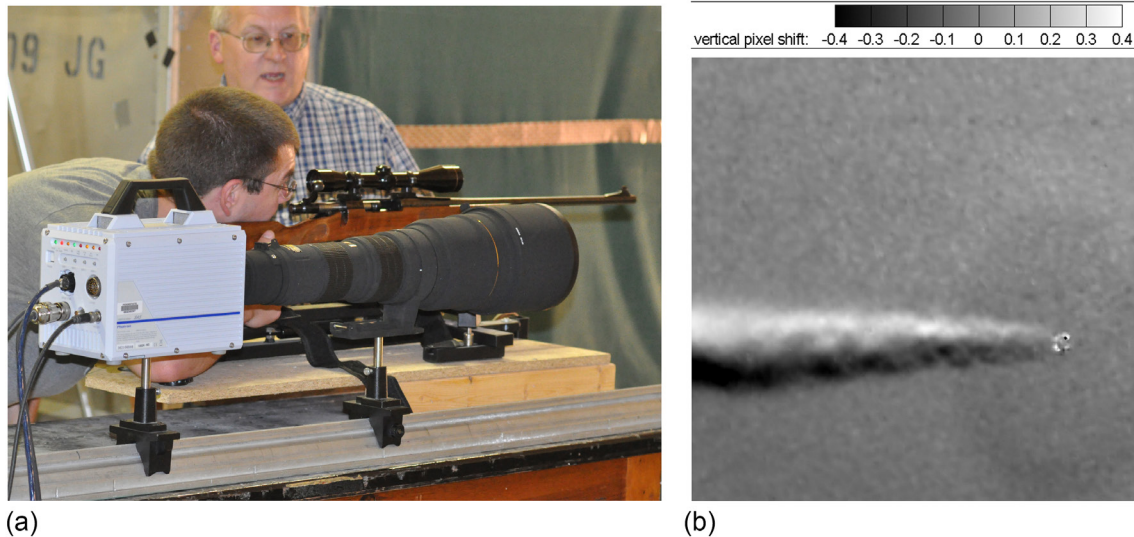
4.4. BOS cameras

In addition to the high-speed and DSLR cameras already discussed in section 2, there is a broad range of scientific CCD and CMOS cameras with speeds up to about 200 fps that can serve for BOS imaging. These cameras often have a direct USB connection with the BOS computer and can interact directly with image processing software.

Raffel [24] notes that conventional cameras (such as consumer-grade DSLRs) can also be used for BOS imaging, but should be set for raw or TIFF (uncompressed) image output. Megapixel-range resolution is required to resolve background features, and a telephoto zoom lens is often needed to provide adequate magnification of *S*, upon which BOS sensitivity depends [60]. BOS also frequently demands high ISO camera sensitivity as well as kW-range floodlight illumination of the background, especially for high-speed imaging and when a lens aperture of *f*/22 or smaller is needed to maintain both *S* and *B* in focus.

4.5. BOS software

There are many software options with which to analyze BOS images. All involve either the traditional pattern-matching cross-correlation approach [24, 61] or the optical flow approach [33, 62–64] taken by the computer vision community. The former is straightforward, relatively foolproof, and almost 'blind,' while the latter is more sophisticated with more input choices and adjustable constants.

Atcheson *et al* [33] compared the gradient-based Lucas–Kanade and Horn–Schunck optical flow algorithms and the variational Brox algorithm with BOS cross-correlation processing using MatPIV, a freeware implementation of PIV in MATLAB™. They found that BOS resolution can be significantly improved by processing image pairs using optical flow algorithms, and with the use of a multiscale background. Smith *et al* [62] found the Horn–Schunck algorithm to yield robust, higher-quality flow results quicker than correlation processing when applied to wind tunnel and flight-test BOS data. Letelier *et al* [63] demonstrated improved BOS resolution using a total variation optical flow approach applied to thermal convection in a Hele-Shaw cell. For processing PIV image pairs, Liu *et al* [64] found improved accuracy

Figure 5. (a) Photo of 30-06 rifle and high-speed camera aimed at distant BOS background, (b) BOS image of bullet wake just after bullet penetrates background.

and much better resolution using optical flow, provided the parameters of the computation are properly selected and there are no significant illumination changes between frames. Overall, the evidence weighs in favor of optical flow despite the simplicity of sticking with BOS image-correlation processing.

Optical flow functions including the Lucas–Kanade and Horn–Schunck algorithms are available in the MATLAB™ Computer Vision System Toolbox and the MathWorks File Exchange. OpenCV computer vision software has optical flow functions, along with many others. NIH ImageJ image processing freeware has both optical flow and PIV plug-ins.

OpenPIV and as many as a dozen other open-source freeware PIV codes are available online. Half are MATLAB™ compatible. Commercial PIV software includes PIVview™ and the flagship codes of the major manufacturers of PIV instrumentation. All of these codes can do image-correlation processing of BOS image pairs as if they were PIV pairs. Even commercial codes like VIC-2D™ by Correlated Solutions Inc., intended for measuring the displacement and strain of solids, are readily adapted to BOS image processing [61]. DigiFlow™ (damtp.cam.ac.uk) software includes a pattern-matching capability specifically written for synthetic schlieren. Most of these cross-correlation codes can measure shifts as small as 0.1 pixel [32]. To use them, one chooses the interrogation window size to exceed the largest expected pixel displacement but no larger, in order to preserve resolution.

Image subtraction was described in section 4.2.2 as a means of creating quick BOS images. For pairs of still images the necessary processing can be handled by commercial software for the consumer such as Adobe Photoshop™, though it is not designed for scientific image processing. NIH ImageJ freeware (https://imagej.nih.gov/ij/) is designed for that, and is immensely capable, as is the MATLAB™ Image Processing Toolbox.

Figure 3(c) shows a subtraction BOS image created in MATLAB from the same lit-candle and tare images used for figure 3(a). After subtraction the result is very dark, and is tone-inverted and contrast-stretched in this example to improve visibility. Figure 3(d) is the image-subtraction equivalent of figure 3(b), showing only refractive-index changes between adjacent frames of a video sequence and therefore revealing turbulent motion but not the laminar candle plume. The results of image subtraction resemble shadowgraphy, where strong refractive-index gradients are the most visible features. For comparison, a tone-inverted candle-plume shadowgram is included as figure 3(e).

This image subtraction approach is attractive for its reduced processing burden, lack of pixel-level analysis, and absence of averaging over a correlation window, which has been shown useful for imaging shock waves [34, 43].

In a broader sense, BOS and the other techniques reviewed here need frequent general-purpose image processing such as contrast stretching, sharpen or blur, and applying a color gradient filter to a monochrome image. This capability is available in Photoshop™ for still images and in ImageJ, MATLAB™, and various video editing software programs. ImageJ, serving the biology community, includes many plug-ins for microscopy. Some are useful here too, since microscopy shares much with schlieren and shadowgraphy [1, 65].

4.6. Examples

In addition to the BOS examples already discussed, figure 4(b) deserves special attention. It gives another view of the NASA T-38 aircraft flowfield, this time seen against the disc of the sun [39]. This is BOS on a truly grand scale, with 11 km distance from camera to S and 150 million km from S to B. When observed through a telescope with a calcium K-line filter (hence the acronym CaKEBOS), the texture of

the sun is revealed and can be used as a well-illuminated BOS background subtending about a ½° angle in the sky. The BOS field-of-view is a circle of some 100 m diameter in figure 4(b). This magnificent schlieren field-of-view does not depend upon the airplane, but could also be visualized atop a hill or mountain by anyone with a telescope, a calcium K-line filter, and BOS processing software (see further discussion in section 10).

Figure 5 shows a BOS visualization that was set up to answer a question raised by military snipers. They saw through their telescopic sights a refractive disturbance in the air following a gunshot that was thought to be due to shock waves. To image this, a high-powered rifle and a high-speed camera (Photron Fastcam SA-5) were mounted side-by-side, figure 5(a). A round was fired through a distant posterboard BOS background backed by a heavy-duty bullet stop. The camera acquired data at 30 000 fps and 1 μs frame exposure through an 800 mm telephoto lens. The BOS image shown in figure 5(b) was captured just after the supersonic round, which entered the field-of-view from the left, penetrated the background. It clearly shows that the only visible refractive disturbance, from the point-of-view of the shooter, is the bullet's turbulent wake.

5. Digital streak schlieren and shadowgraph imaging

Before the digital revolution, streak schlieren images and shadowgrams were exposed through a slit onto the rotating drum of a high-speed film camera without a framing mechanism [1]. Some streak cameras still follow this principle with the film now replaced by a digital sensor.

The high-speed video cameras described in section 2.1 are all framing cameras without a direct mechanism to produce a streak image. Many of them do, however, segment their image planes to get high frame rates. Segmented images at a million fps may be only a dozen pixels tall and many more pixels wide. These slit-like images are best suited to 1D unsteady phenomena, where changes take place primarily in one spatial dimension. Explosions, gunshots, impact phenomena and shock wave propagation through materials are a few subjects that can be studied this way. Textbooks (e.g. [66]) describe them using *x–t* diagrams (spacetime diagrams, wave diagrams), where the progress of something moving in the prevalent direction *x* is plotted versus time *t*. Streak-schlieren images from the film era were, in fact, analog *x–t* diagrams, e.g. [4, 67]. There and in the digital streak schlieren method described here, the slope of a line has the physical dimension of distance/time, or speed.

Around the dawn of high-speed digital video, Katayama [68, 69] suggested extracting a pixel row from each of a sequence of images, then stacking these extracted rows to form a new image in which the stacking direction becomes a time axis. He claimed that this 'presents a set of captured high-speed images in a way that encourages new insights into the event under study.'

One of the first digital streak shadowgrams, shown here as figure 6, did not come along until 2010 [70]. It shows the explosion in free air of a ~1 g composite PETN/RDX charge over a radius of ½ m and a time interval of 3/4 ms. The explosion produces light for the first few microseconds, after which one observes the expansion and contraction of relatively-cold gas and its attendant shock waves. The primary shock begins strongly, Mach 8 or 9, but quickly asymptotes toward the slope of a sound wave as it leaves the visible frame in figure 6. The gaseous products of combustion appear almost opaque in this figure, but the shape of their upper boundary in spacetime yields useful data.

Today, streak schlieren analysis continues to be used in explosives research [71, 72], and has expanded to measurements of the impact shock-Hugoniot response of polymers [73, 74], oscillating supersonic cavity flows [75–77], and fire research [50].

There is no commercial software available to make streak schlieren images, but a simple MATLAB™ script can do this using a `for` loop defined by `for i = 1:1: endpicnumber;` where `endpicnumber` is the number of images in the sequence of interest. Inside the loop, read in each sequential image and use it to fill the 3D matrix `pic` using `imread`, then create a new 2D image matrix `streakimage` by adding a row to it for every value of `i` using
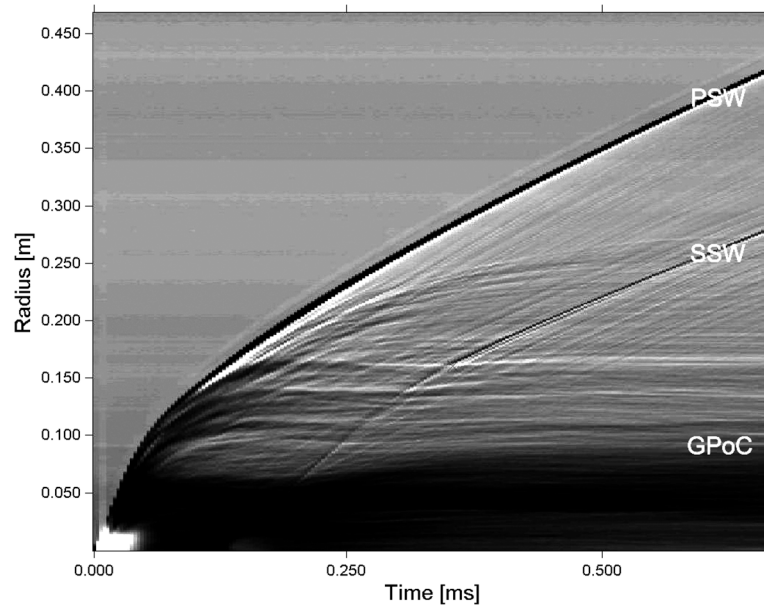
```
streakimage(i,:) = pic(r_center,c_center:
size(pic,2));
```

`r_center` and `c_center` are the row and column numbers in the input images where `streakimage` will begin.

Closely related to streak schlieren and shadowgraphy is shock tracking, in which no streak image is made but the location of the primary shock wave from an explosion or an unsteady shock in a supersonic inlet, for example, is automatically located in each frame of a high-speed digital video sequence and then extracted and plotted as useful quantitative spacetime data. Examples from explosives research are shown in [78, 79]. Timmerman *et al* [80] describe an algorithm for the automatic digital detection of a shock wave in a shadowgram based on its characteristic light-dark boundary.

Another closely-related topic is slit-scan schlieren imaging [1, 81], in which a digital line-scan or time-delay-integration camera is focused on a distant light-dark boundary. Objects must move across the direction of the slit in order to be imaged, and the schlieren effect is produced by distortion of the background. A simple demonstration of this can be seen on an iPhone camera running a slit-scan app [82].

A notable light-dark boundary for slit-scan schlieren is the solar limb, used for imaging flying aircraft by Weinstein [81], NASA and Spectabit Optics LLC [83]. The latest digital manifestation of this approach is called Synthetic Limb Edge Schlieren (SLES), which was used to image the take-off of a 737 jetliner in figure 7. The jet exhaust is obvious in this figure, but more-subtle features of the flow such as turbulent landing-gear wakes can be seen as well. Like the calcium-K-line BOS shown earlier in figure 4(b), SLES also

Figure 6. Streak schlieren image of the explosion in free air of a ~1 g composite PETN/RDX charge. PSW = primary shock wave, SSW = secondary shock wave, GPoC = gaseous products of combustion [70].

has non-aeronautical applications. It can be adapted to rocket-sled slit-scan schlieren imaging, for example [81], or even to automobiles.

6. Schlieren velocimetry

Schlieren velocimetry was invented by Townend in 1936 [84], many decades before high-speed digital video and computerized numerical analysis made it practical. It uses refractive turbulent structures, visualized in schlieren or shadowgraph images, as Lagrangian tracking 'particles' for a PIV-like analysis of flowfield velocities [21, 85]. The technique requires that a flow be 'seeded' with turbulent eddies that can be tracked through sequential schlieren images, at least for a very short time interval Δt, as if they were particles. Compressible turbulent flows are ideal for schlieren velocimetry because their naturally-occurring refractive turbulence can be easily visualized, recorded by a high-speed camera, and tracked using computer algorithms. Deliberate 'seeding' can be done in some other scenarios by adding a passive refractive scalar to the flow, as demonstrated in [85] where a low-speed boundary layer is thermally seeded by a heater mounted in the wind-tunnel floor.

Early implementations of schlieren velocimetry used pattern-matching algorithms or optical flow to track turbulent eddy motion or other motion in supersonic shear layers [86] and gas plumes [87]. Jonassen *et al* [21] extended the technique to the measurement of a turbulent helium jet using a PIV camera, pulsed laser or strobe illumination, and commercial PIV image-correlation software to track the turbulent features between sequential image pairs. They discovered an important limitation of schlieren velocimetry: that velocity measurements in schlieren images are path-integrated (equation (2)) in the same manner as are refractions. For the round turbulent jet they measured, Jonassen *et al* [21] used the Abel transform to relate the

path-averaged schlieren velocity field to the centerline velocity of their axisymmetric turbulent jet flowfield as measured by traditional PIV, and observed good agreement. For planar 2D flows such as wind tunnel boundary layers, schlieren velocimetry with the light path parallel to the wall provides reasonable mean-velocity results directly without a path-averaging correction.
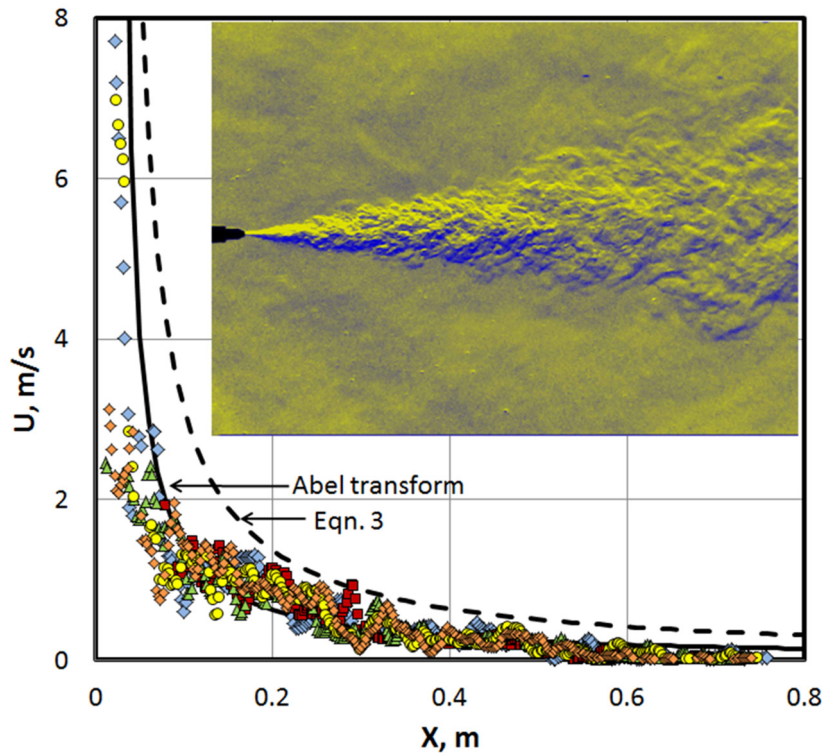
If a pulsed LED light source or a high-speed video camera, as described in secs, 2 and 3, had been available for the experiments of Jonassen *et al*, it would have made a big difference. In figure 8 we show a similar but more recent example, the round turbulent jet produced by propane gas mixing with air. This was imaged by a Photron Fastcam camera that produced megapixel schlieren images at 3000 fps, exposed at 33 μs/frame. The 1 m aperture single-mirror schlieren system ([1] section 4.1) was set for reduced sensitivity and extended measuring range by using a 5 mm graded filter in place of a knife-edge, following the advice of Jonassen *et al* [21] to avoid over-ranging the schlieren optics for velocimetry work. (If the measuring range of the system is exceeded, entire regions of the image become 100% bright or dark [1].) A single colorized schlieren frame of the propane jet is shown as an inset in figure 8.

Five image pairs with frames $\Delta t = 1$ ms apart were chosen at random from several thousand captured by the camera. Jet centerline velocity data were extracted from each pair using a commercial 2D image-correlation code intended for displacement measurements in materials testing. The results are given 5 different symbols in figure 8 and are plotted as velocity U versus distance x along the jet centerline from the nozzle exit. The scatter band of these data is largely because each image pair yields a different 'snapshot' of a turbulent flow. Their average, however, indicates $U \propto 1/x$ behavior.

The dashed line in figure 8 is the mean-flow similarity law for round turbulent jets, (based on equation (5.6) from [88]):

Figure 7. Takeoff of a 737 jetliner as visualized by Synthetic Limb Edge Schlieren (SLES). Reproduced with permission from Spectabit Optics LLC.

Figure 8. Schlieren image of propane gas jet mixing with air (inset), and plotted results of jet centerline velocity U_{CL} versus distance from nozzle exit x obtained by schlieren velocimetry analysis of pairs of such images. See text for full description.

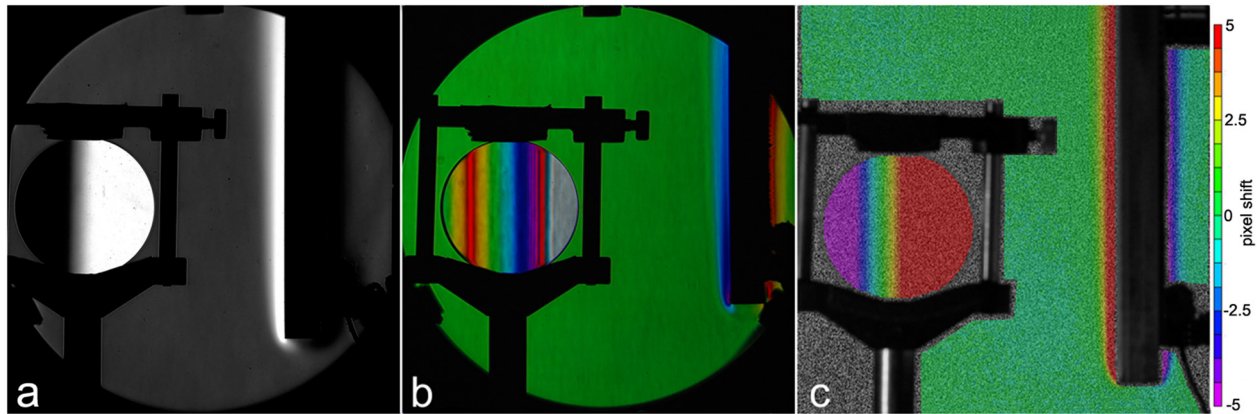$$\frac{U_{CL}(y)}{U_j} \propto \frac{d}{y} \qquad (3)$$

Where $U_{CL}(x)$ is the centerline velocity and U_J and d are the jet exit velocity and nozzle exit diameter: 54.8 m s^{-1} and 0.75 mm, respectively, for this $Re_d = 7460$ jet.

The discrepancy between the schlieren velocimetry data shown in figure 8 and the dashed line from equation (3) is mainly due to optical path averaging across the axisymmetric jet. The Abel transform of the Gaussian mean-velocity profile [88, 89] of a round turbulent jet predicts that schlieren velocimetry will measure a centerline velocity that is only about 46% of the actual $U_{CL}(x)$ given in equation (3). That is plotted as a solid line in figure 8, which agrees with the velocimetry data only in the $0.2 < x < 0.5$ m range.

This points to another schlieren velocimetry issue: the choice of Δt for a flow having a broad range of velocities. The present Δt is much too long to measure the high-velocity

region near the nozzle exit. The image correlation returns values too small, or else fails altogether in that region. Likewise Δt is too short for $x > 0.5$ m, where the image correlation detects essentially no motion and returns zero velocity. Thus flows like the present example, with a 2-to-3-order of magnitude mean velocity range, require schlieren velocimetry with several different Δt values in order to carry out a complete measurement.

Hargather *et al* [85] attempted to address the path-integration issue using a focusing schlieren technique to achieve an ideal planar velocity measurement. The focusing schlieren optics worked well to limit the refractive imaging to a depth of focus of about ±40 mm. A narrower depth of focus, however, was found to be untenable due to the loss of schlieren sensitivity with decreasing focal depth. Schlieren velocimetry, therefore, will always require some degree of path averaging by the nature of visualizing refractive fields.

Figure 9. Schlieren setup with a free-convection boundary-layer on a flat plate (right) and a standard lens (left) for quantitative measurements: (a) monochromatic schlieren, (b) rainbow schlieren, and (c) BOS [35].

The boundary layer study in [85] also identified a second limitation of the technique: turbulent intermittency results in a lack of 'seeding' in the flow, similar to insufficient particle seeding in a PIV experiment. The turbulent boundary layer velocity measurement failed upon approaching the outer edge of the boundary layer ($y/\delta > 0.6$), where the turbulent structures become very intermittent with an undisturbed freestream flow having no visible turbulent structures. This dearth of turbulence resulted in poor statistics for velocimetry and a low average velocity measurement followed.

The schlieren velocimetry concept has been applied successfully using a range of imaging techniques and measurement scales including shadowgraphy [90], schlieren [91], and BOS [24, 50, 92]. The choice of imaging technique is setup- and application-dependent, but shadowgraphy has the advantage of producing crisp turbulence details without over-ranging as schlieren optics can, which allows better automated image-correlation analysis [21]. Since turbulence is being tracked, turbulence measurements as well as mean-flow measurements can be made. Some examples include [93–95].

The computer processing of schlieren velocimetry images follows the same general algorithm choices as those described for BOS in section 4. Richard and Raffel [26] note that BOS is readily combined with PIV. Commercial PIV or other digital image-correlation software has been used with success, but these codes are designed to detect the motion of points in a field and can be confused by schlieren or focusing-schlieren images with more-smoothly-varying grayscale values. Correlation and optical flow algorithms built into MATLAB™ are preferred by some who write their own routines [85], or who use open-source libraries and functions such as *SubME* [91, 96].

The limitations of path averaging, turbulent intermittency and the restriction to refractive flows presently prevent schlieren velocimetry from rivaling PIV as a dominant velocimetry approach. However, it can be useful for studying flows where traditional particle seeding cannot be implemented, including, for example, some hypersonic wind tunnels. Schlieren velocimetry also generally tracks the fine turbulent substructure better than the large, formally-defined turbulent structures that can propagate at speeds different from the local convective velocity [97]. Overall, schlieren velocimetry remains a work in progress that provides a niche measurement capability.

7. Quantitative analysis of schlieren images

Some of the quantitative measurements obtainable from schlieren images have already been discussed, including velocimetry and shock wave tracking. Here we describe the quantitative evaluation of gas density from the refractive-index-gradient field in a schlieren image. Such density measurements were once the sole domain of laser interferometry, since schlieren data required integration. But now the integration and subsequent processing can be done with ease on a laptop computer, and quantitative schlieren methods, having distinct advantages over interferometry in terms of simplicity, image quality (no coherent artifact noise) and vibration resistance, are enjoying a renaissance. The modern techniques of quantitative monochrome schlieren, rainbow schlieren, and BOS were reviewed recently in detail by the present authors [35], so only a limited overview is given here.

Quantitative schlieren imaging relies on the ability to relate an imaged refractive index gradient, in the form of a pixel intensity or hue, to a known refraction angle. The simplest approach to this is to place a calibration object with a known refractive index variation in the field-of-view, thus allowing a direct conversion from image pixel intensity to a corresponding refractive index gradient value. Typically a simple lens with known diameter and (long) focal length is used [4, 35]. Figure 9(a) shows this 'standard' calibration lens (10 m focal length) positioned in the schlieren field-of-view along with a heated vertical flat plate on which the 2D free-convection thermal boundary layer is being measured. Each radial position in the lens has a different refractive index gradient, or refraction angle, in order to have

the effect of focusing incoming parallel light across the entire lens surface to a single point. The imaged horizontal gradient across the lens in figure 9 provides the necessary calibration of pixel intensity to refractive-index-gradient value.

The gradients are imaged only horizontally across the boundary layer in figure 9 by using a vertical schlieren cutoff. The choice of focal length for the calibration lens provides quantification of various ranges of schlieren sensitivity, with longer lenses providing finer resolution of refractive index variations. The calibration lens focal length must also be larger than the focal length of the main schlieren optics.

Once the refractive-index-gradient field is quantified in this manner, it is then numerically integrated to produce the refractive index field, which is converted to fluid density via the Gladstone–Dale relationship, equation (1) [1, 35]. The conversion to density requires that the imaged fluid is uniform with a known Gladstone–Dale constant k. Quantification of the density in a mixture of gases would require an estimate of the Gladstone–Dale constant for the mixture. Further quantification to temperature, pressure, or concentration measurements depends on a detailed knowledge of the gas species present as well as other flow properties. If only a single gas is involved, a simple state equation is used to determine temperature from density if the pressure is known, or vice versa [35, 98]. Evaluating gas mixtures this way requires accounting for variations in refractive index among the gases involved.

Rainbow schlieren, figure 9(b), uses a color-grid cutoff in place of the traditional knife-edge to produce images with hue variations in place of grayscale values. Schardin [4] originated the idea, but the term 'rainbow schlieren' was introduced by Howes [99, 100] to describe the colorful images produced by the continuous-color-spectrum cutoff. It has received wide attention from researchers [13, 101, 102] for quantitative measurements, whereas its grayscale antecedent (figure 9(a)) has had comparatively little use.

The colors of the rainbow schlieren cutoff do not actually provide more information than the grayscale knife-edge. Light ray bending angles are simply indexed by the hue they pass through in the cutoff plane rather than the grayscale degree-of-cutoff by a knife edge. Rainbow cutoffs do, however, have the advantage that they can be designed to color-code specific refraction directions or magnitudes, e.g. a bulls-eye pattern to highlight radial refraction magnitudes or a four-quadrant grid to resolve 2D refraction directions and magnitudes. Digital color images also inherently provide more information-coding capability than grayscale, so rainbow schlieren can have a broader measurement range than grayscale schlieren in principle. Disadvantages include a resolution loss due to diffraction by the narrow color cutoff bands and future fabrication problems of precision rainbow cutoff filters requiring color transparency film, mentioned earlier.

The BOS technique, figure 9(c), is inherently quantitative if the setup geometry is known, therefore no calibration lens is required, although we have included one for comparison in the figure. The image-correlation processing that produces a BOS image provides both the magnitude and direction of a 'pixel shift' image distortion. This pixel shift can be directly

quantified to a refraction angle using simple trigonometry and the geometry of the setup (figure 1(d)), including the system overall length, position of schlieren object S, and camera pixel resolution [35]. Many groups have applied quantitative BOS for density measurements and even tomographic reconstruction of density fields [29, 30, 32, 36, 57, 103, 104].

BOS is unique in that the measurement resolution and range can be adjusted easily by increasing the camera resolution or by displaying the results of only a limited image area. For example the lens in figure 9(c) shows a limited banding region because that was the chosen refraction range (see the horizontal pixel shift legend on the right side of figure 9(c)) for the free-convection boundary layer under study. The user can adjust the displayed BOS output to provide a desired image sensitivity.

Because of non-parallel illumination in the typical BOS setup (figures 1(d) and 9(c)), the optical axis must coincide with the surface of the heated plate in figure 9(c) in order to avoid measurement errors. Figures 9(a) and (b), in contrast, were produced by a parallel-light *z*-type schlieren system as diagramed in figure 1(b). With that equipment the 2D heated-plate flow and calibration lens may be placed anywhere within the circular field-of-view.
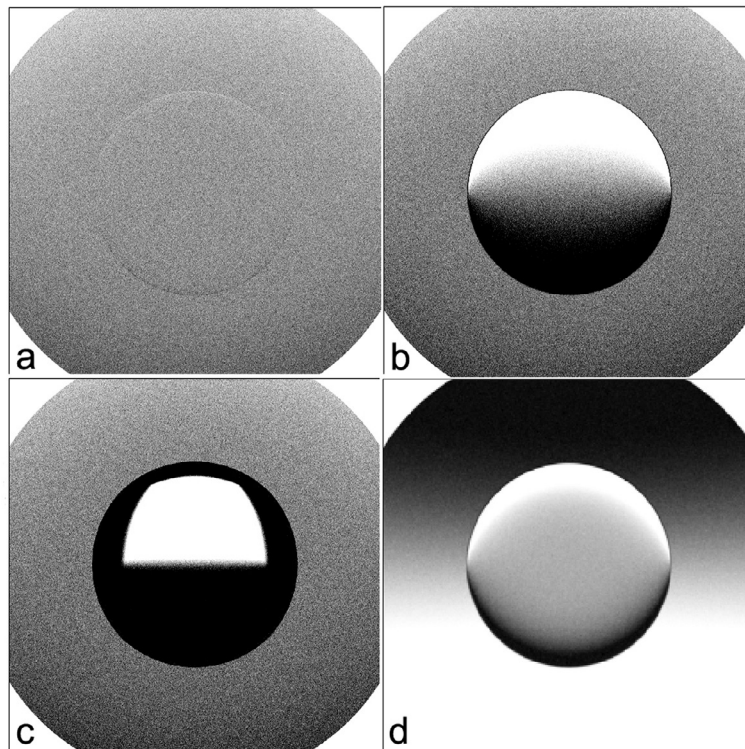
An important future direction of quantitative schlieren techniques is in the tomographic reconstruction of more-general 3D density fields, for example [105], which used 20 lens-type schlieren systems similar to figure 1(a) to simultaneously image a 3D flow from 20 different directions. As camera technology continues to improve and researchers have access to more cameras at less cost for imaging a single experiment, as well as better computing resources, tomographic density reconstruction from multiple BOS images will become standard. While the details of the current state-of-the-art in multi-camera 3D BOS are beyond the present scope, this topic was recently reviewed by Raffel [24].

8. Computer simulation of schlieren and shadowgraph optics and images

8.1. Simulation of the optics

'Ray-tracing' software has grown up over the last 15 years. There are at least 50 programs now available, some commercial and others freeware [106]. To demonstrate the capability of current ray-tracing optical design programs, a simulation of a small *z*-type schlieren system (figure 1(b)) was run on Zemax™ (zemax.com) with ray-tracing but no diffraction effects. Twin spherical mirrors of 54 mm diameter and *f*/21 are offset from the optical axis by opposing 4° angles. (For this diameter and *f*/number there is no practical difference between spherical and parabolic mirrors [107].) A small (sub-millimeter) non-coherent light source LS is used in this simulation, and a horizontal knife-edge KE is placed in the cutoff plane with 50% cutoff.

In the center of the test region between the mirrors a spherical schlieren object S is simulated, having a diameter of 25 mm. A corresponding physical experiment would involve a soap bubble filled with a gas more refractive than the

Figure 10. Images generated by a ZEMAX simulation of a *z*-type schlieren system having a spherical schlieren object of different refractive index *n* than the surrounding $n_{ambient} = 1.000\,293$. (a) $n = 1.000\,294$, (b) $n = 1.000\,393$, (c) $n = 1.001\,293$, and (d) $n = 1.000\,393$ with the knife-edge displaced 10 mm from the beam focus along the optical axis.

surrounding air, which was assumed to have a refractive index $n_{ambient} = 1.000\,293$. The refraction theory for this example schlieren object is given by Weinstein [81].

Using this simulated schlieren system, one-megapixel schlieren images are produced in Zemax™ by specifying a large number of light rays, in this case 50 million. Each of the four simulations in figure 10 required a few minutes to complete on an ordinary laptop computer.

In figure 10(a) the refractive index inside the sphere *S* is set at 1.000 294, a very small change from the ambient value producing a barely-visible effect in the simulated schlieren image. Increasing *n* to 1.000 393, however, has an obvious effect in figure 10(b), similar to filling the soap bubble with ammonia gas in a corresponding physical experiment. In figure 10(c) the refractive index of *S* is further increased to 1.001 293, which grossly over-ranges the schlieren system. Finally in figure 10(d) the case of figure 10(b) is repeated with the knife-edge displaced 10 mm along the optical axis from the beam focus, thus producing uneven schlieren background illumination. Also in figure 10(d) the number of computed rays was increased to 100 million, which eliminates most of the grainy background noise seen in figures 10(a)–(c).
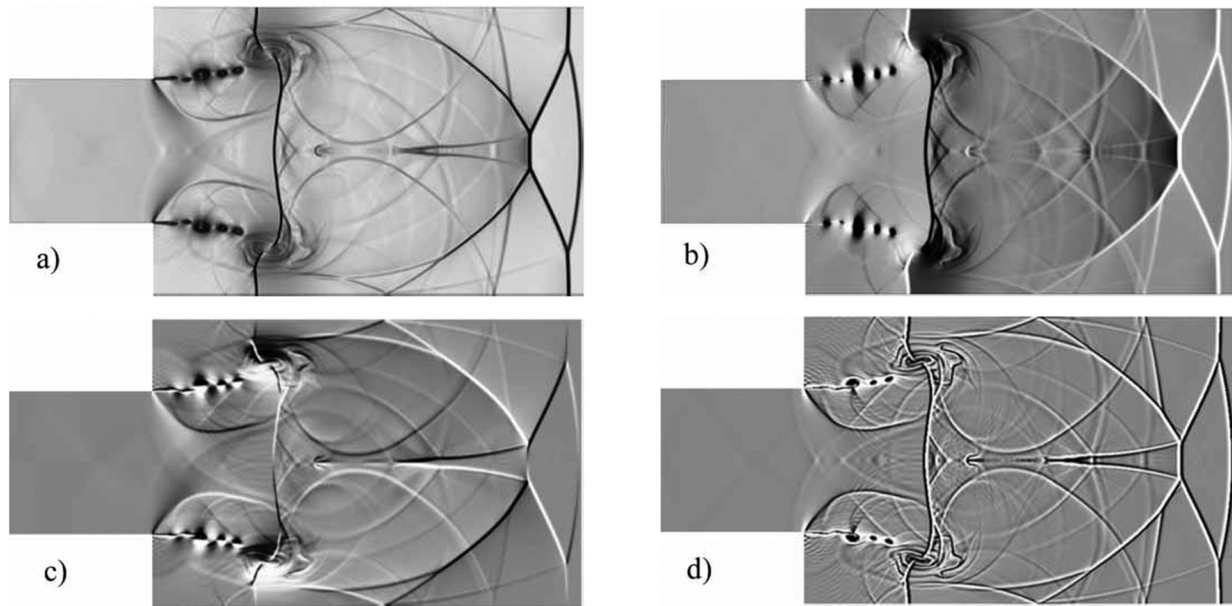
It was further observed in these simulations, despite the large *f*/number of the mirrors and their small off-axis angles, that Zemax™ correctly predicts a slight astigmatic aberration causing the schlieren beam to come to focus as a horizontal (saggital) line and a vertical (tangential) line at different locations along the optical axis.

This example demonstrates that it is possible to design and optimize a schlieren apparatus with a detailed simulation of its performance, using modern optical design software such as Zemax™, before the physical instrument is actually fabricated. Moreover, the software contains a library of stock commercial optics that can be chosen as components during the design. In that case the software output includes a parts list and cost estimate for fabricating the instrument. Further reading on this topic can be found in [29, 108–110].
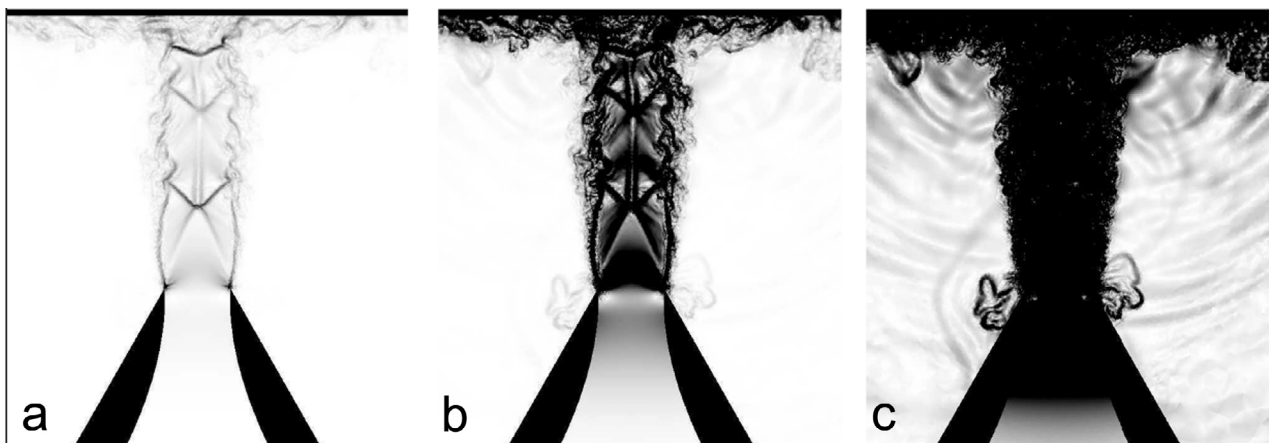
8.2. Displaying CFD results as computer-simulated schlieren images and shadowgrams

CFD is increasingly turning to schlieren and shadowgraphy as a paradigm of visual presentation in the post-processing of numerical flow simulation data. The idea effectively began with Yates 24 years ago [111, 112], and has gathered momentum ever since [77, 113–117]. Currently, many authors barely mention why their results are displayed as derivative fields. The striking visual appearance of schlieren and shadowgraph images is apparently ingrained in the scientific community, so the presentation of density gradients—instead of just the density itself—has become an obvious and logical choice.

Many researchers compare computed schlieren images directly with experimental schlieren images having the same flow conditions in order to validate the computation (or the experiment, or both) [113, 117–119]. Other researchers use schlieren and shadowgraph images to present intricate

Figure 11. Images from a numerical solution of a supersonic jet-exit flowfield, rendered as (a) bright-field schlieren, (b) vertical-knife-edge schlieren, (c) horizontal-knife-edge schlieren, and (d) shadowgraphy, from [122] courtesy A Hadjadj, reprinted by permission of the publisher (Taylor & Francis Ltd, www.tandfonline.com).

Figure 12. Computed schlieren images from a numerical solution of an impinging turbulent supersonic jet, (a) $0 \leqslant \nabla\rho \leqslant 1000$ kg m^{-4}, (b) $0 \leqslant \nabla\rho \leqslant 100$ kg m^{-4}, and (c) $0 \leqslant \nabla\rho \leqslant 10$ kg m^{-4}, from [124] courtesy A Dauptain, reprinted by permission of the publisher (American Institute of Aeronautics and Astronautics, www.aiaa.org).

simulation results visually [120–122]. Here we show in figure 11 an excellent example by Hadjadj and Kudryavtsev [122] in which the same numerical supersonic jet-exit flowfield is rendered as (a) bright-field schlieren (circular cutoff), (b) vertical-knife-edge schlieren, (c) horizontal-knife-edge schlieren, and (d) shadowgraphy. The $|\nabla\rho|$ or bright-field schlieren, figure 11(a), is often used to show numerical results following the suggestion of Quirk [123], but for good reasons it is seldom used in experimental practice compared to the standard knife-edge cutoff [1]. Note also that the shadowgram (figure 11(d)) does a better job of revealing vortex-core details than any of the schlieren images shown, due to its second-derivative sensitivity.

Dauptain *et al* [124] provide another excellent computed schlieren example, shown in figure 12, in which the schlieren

sensitivity is systematically varied in sequential images to investigate the flow features of an impinging turbulent supersonic jet computation. In figure 12(a) the schlieren measuring range is very broad, $0 \leqslant \nabla\rho \leqslant 1000$ kg m^{-4}, and the sensitivity is quite low. Mainly shock waves in the jet are visible but little else. In figure 12(b) the range is reduced by an order of magnitude to $0 \leqslant \nabla\rho \leqslant 100$ kg m^{-4} with an attendant sensitivity increase, and details of the shear layers and wall jet now appear while the jet shocks become over-ranged. Finally, in figure 12(c), the range is reduced by another order of magnitude to $0 \leqslant \nabla\rho \leqslant 10$ kg m^{-4}, over-ranging everything inside the jet but making visible the acoustic radiation associated with the jet impingement. This clever experiment could actually be done with real optics and a real impinging jet, but schlieren images over 3 decades of measuring range variation

Figure 13. Large-scale retroreflective shadowgram showing thermal effluent from outdoor cooking on a grill, reproduced with permission from FloViz Inc.

are seldom taken in physical experiments. More often the degree of knife-edge cutoff is not considered to be a variable.

9. Retroreflective shadowgraphy

Edgerton (1903–1990) of MIT is famous for having invented the electronic flashlamp or strobe lamp [125]. Sixty years ago he also demonstrated a simple and elegant direct-shadowgraph technique for imaging large-scale high-speed events like explosions and shock waves [126]. Only a retroreflective screen, brief illumination, and an ordinary view-camera of the period were required. To demonstrate its robustness, Edgerton photographed the shadowgram of a detonator explosion outdoors in daylight using one of his strobe lamps for illumination.
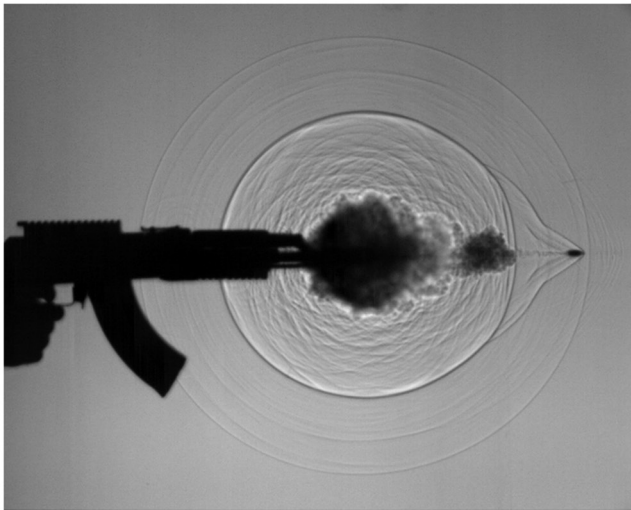
Very little attention was subsequently paid to Edgerton's retroreflective shadowgraph technique during the 20th century. It saw only incidental use in aeroballistics, e.g. [127], and helicopter rotor testing [128, 129], but now it enjoys a reawakening. We have recognized Edgerton's role as inventor by referring to the combination of direct shadowgraphy (figure 1(c)), a retroreflective screen SC, and modern high-speed imaging as 'Edgerton retroreflective shadowgraphy' [130].

Direct shadowgraphy with diverging illumination, first practiced by the infamous Jean-Paul Marat ([1], ch 1), was improved by Edgerton who cast his shadowgrams on a retroreflective screen. The resulting gain in camera image intensity is crucial for high-speed imaging of rapid events such as explosions and moving shock waves. As sketched in figure 1(c), transparent schlieren object S is located about halfway between a small bright light source LS and a retroreflective screen SC, casting a shadowgram on the screen. The diameter of the field-of-view at S can be roughly half that of
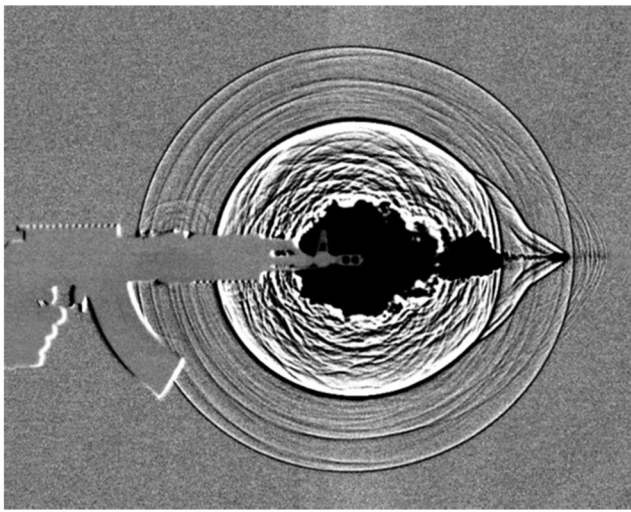
the screen SC. The purpose of the camera in figure 1(c) is to photograph the retroreflected shadowgram that is cast on the screen. If the camera is slightly offset from the light source as described by Edgerton and shown in figure 1(c), then any solid objects in S will be slightly double-imaged in the resulting shadowgram. Alternatively a beamsplitter was used in aeroballistics ranges [127] to eliminate double-imaging by providing exactly-coincident camera and illumination directions. A better solution was found by Hargather and Settles [130] for intense arc-lamp illumination: reflecting the light source focus from a small rod-mirror centered ahead of the camera lens.

Modern high-speed digital cameras and light sources, described earlier, provide the essential new elements in this simple, robust optical technique for imaging large-scale phenomena outdoors as well as indoors. For the retroreflective screen, 3M Scotchlite™ 7610 High Gain Reflective Sheeting material has proven the most successful in the past, returning some 900 times as much light as a perfectly diffusing white surface. Scotchlite™ 3000X Very High Gain Sheeting was also used in wind-tunnel tests at NASA-Langley Research Center [46], but it was ill-suited to the wind-tunnel environment.

Explosions, gunshots, and harsh environments are natural subjects for study by the Edgerton retroreflective shadowgraph technique [73, 130–135]. It has also found application inside the test sections of large high-speed wind tunnels [46, 136, 137]. It can be used to image droplets or bubbles propagating in a large transparent water tank. Even low-speed turbulent thermal convection currents are amenable: In 2005 an ASTM standard was written requiring the use of schlieren or shadowgraph imaging to assess the performance of commercial kitchen exhaust ventilation systems [138]. Lens-and-grid schlieren systems have been constructed for this purpose [1, 81], but shadowgraphy is simpler and just as effective. At

(a)

(b)

Figure 14. (a) raw retroreflective shadowgram from a high-speed video sequence of firing an AK-47 assault rifle, (b) same image following tare subtraction and contrast stretch.

least one large kitchen ventilation manufacturer has put it to good use in new product design and advertising [139, 140]. A retroreflective shadowgram of outdoor cooking on a grill is shown in figure 13.

Due to their similarities, it is natural to ask whether shadowgraphy or BOS is better for a given application. BOS is a better choice for flows with weak gradients, quantitative work, and taking advantage of large natural backgrounds. Shadowgraphy excels at revealing shock waves and thermal turbulence, and produces a ready real-time display without computer processing delay. Its retroreflective screen is likely to be more expensive than a BOS background of the same size, but not nearly as expensive or fragile as a large precise parabolic mirror.

Finally, note that retroreflective shadowgrams are inherently of low contrast, requiring a contrast stretch for good visibility. This is easily done for single images using the image-processing software described in section 4.5, or for real-time video by tare image subtraction, similar to the

procedure described for live BOS processing in section 4.2.2. Figure 14(a) shows a single 1 μs frame from a Photron Fastcam sequence of the firing of an AK-47 assault rifle as seen by Edgerton shadowgraphy. A tare image was taken from this sequence just before the gunshot began, and was subtracted from figure 14(a) and contrast-stretched to yield figure 14(b). This procedure brings out a wealth of weak-shock-wave detail. The shadow of the weapon itself would disappear during the subtraction, except that early recoil has shifted it slightly, causing bright and dark outlines to form around it. This example used a rod-mirror to avoid parallax [130] and a 3×3 m retroreflective screen located about 6 m behind the plane of the gunshot. At this scale, Edgerton shadowgraphy is clearly able to reveal an impressive level of detail.
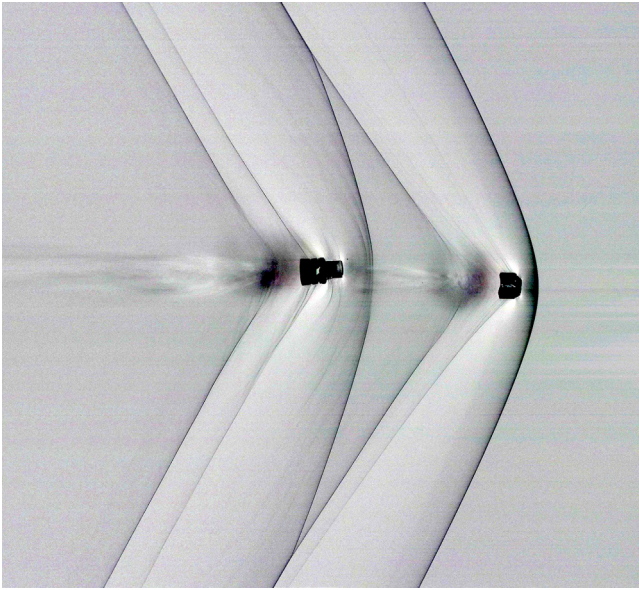
10. Commercial shadowgraph and schlieren instruments

The paucity of commercial shadowgraph and schlieren instruments remains a mystery, especially since their sister instruments, telescopes and microscopes, are such big commercial successes. Who would outfit a new laboratory with a homemade microscope? Yet homemade schlieren instruments are the rule in the West, and there is no evidence that standard schlieren instruments like the IAB-451 [1] are still being produced in Russia. The do-it-yourself tone of this review reflects how far schlieren and shadowgraphy are from plug-and-play. Nevertheless there are currently a few commercially-available instruments, summarized below.

The Aerolab Corporation offers *z*-type parabolic-mirror schlieren equipment in various sizes as instrumentation for its line of research-and-educational high-speed wind tunnels. A benchtop *z*-type system is also produced for the university market, typically with a 76 mm aperture, separate transmitting and receiving modules, and a DSLR or scientific camera for schlieren image viewing and capture. Photos of these instruments can be seen on Aerolab's web page (Aerolab. com).

FloViz Inc. (flovizinc.com) manufactures both lens- and mirror-type schlieren instruments as well as retroreflective shadowgraph equipment. The latter is available in both a portable model with a small field-of-view and a laboratory model with a retroreflective screen up to 3×3 m in size. A 'Foucault schlieren system' is offered as a benchtop instrument consisting of a single spherical mirror of typical 250 mm diameter and an LED light source/knife-edge/ camera unit separately tripod-mounted. Figure 2 was photographed with such an instrument, while figures 13 and 14 were obtained with the laboratory-scale retroreflective shadowgraph instrument just described. BOS instrumentation and design services for related instruments are also available.

Spectabit Optics LLC (Spectabit.com) offers for sale an SLES system and associated software that was described in section 5 and was used to take the aircraft schlieren

Figure 15. Schlieren image of transonic shotgun slug separation made with digital synchroballistic camera [141]. Reproduced with permission from Spectabit Optics LLC.

image shown in figure 7. They also offer a galvanometer-mirror slit-scan streak camera designed for rocket-sled and ballistic-range research [141]. Figure 15 is a schlieren image of transonic shotgun slug separation made with this camera.

Spectabit Optics also markets several versions of a focusing schlieren system, similar in principle to figure 1(e) but improved by the projection of the image of a source grid onto a screen or wall rather than using the physical source grid SG shown in the figure. This approach is also known as 'projection schlieren,' and is described by Weinstein [81]. In Spectabit's Digital Schlieren System the projected source grid is digitally manipulated in order to match a fixed cutoff grid [142], thus ameliorating the troublesome grid alignment chore in earlier analog focusing schlieren systems [1] as well as removing the need for photographic film cutoff grids. It was mentioned in section 2.3 that the demise of sheet film (and the rise of BOS) has made large traditional focusing schlieren systems obsolete, but the digital version lives on.

Figure 16(a) is a photo of a Spectabit projection schlieren instrument with a hot teakettle as a test object. On the right in figure 16(a) is the digital projector that projects the source grid onto a wall-mounted screen and the resulting schlieren image on a laptop computer in the foreground. Figure 16(b) is an example teakettle schlieren image produced by the device.

Finally, Spectabit's commercial software package SchlierenView™ captures and enhances still images and live schlieren video from a range of common camera platforms. The cited example of background-subtraction BOS [51] was accomplished with this software and an ordinary webcam and laptop computer.

More technical detail on the schlieren instruments marketed by Spectabit Optics is found on their website and in Trolinger *et al* [143].

(a)

(b)

Figure 16. (a) Photo of Digital Schlieren System with hot teakettle as test object, (b) resulting schlieren image. Reproduced with permission from Spectabit Optics LLC.

11. Conclusions and outlook

A few miscellaneous topics that did not fit the above framework need to be mentioned:

1. The plenoptic or light-field camera was introduced during this period, and was tried out in combination with schlieren optics [144–146]. Its immediate relevance is to tomographic schlieren and to BOS, especially for strongly-refracting objects and with simultaneous background and test object in focus. This topic bears watching for future developments.
2. The schlieren imaging principle has been applied to electron microscopy of weak phase objects [147, 148].

3. An inexpensive adjustable replacement for the Wollaston birefringent prism was invented, and is found useful in schlieren interferometry [149]

Schlieren and shadowgraphy have always been visualization tools first and quantitative measuring instruments second. That is still true, but the last 15 years has brought about their digitization. BOS is the first such method that depends on computer vision and image processing in order to function. BOS is not a general replacement for traditional schlieren optics, on account of its several limitations, but it has established an important role of its own.

The image processing and handling power of MATLAB™ and similar languages now facilitates many quantitative aspects of schlieren and shadowgraphy that have been possible for decades in principle, but were just too cumbersome to be useful before. Now that there is this capability, it is important to remember to capture digital images in uncompressed full-size raw or TIFF format, and to always shoot tare images for use in subsequent processing.

As taught by figures 11 and 12, useful flow explorations can be done by applying schlieren and shadowgraph principles to the results of a CFD solution.

For the future, we need to be aware of developments in computing, optics, electronics, and robotics that resonate with schlieren and shadowgraphy. Useful new LEDs and laser diodes will appear, including white-light pulsed lasers. BOS will establish important applications of its own in tomography, industrial airflow imaging, leak detection, and perhaps even helping pilots to detect thermals, wakes, and clear-air turbulence.

Some of the do-it-yourself MATLAB™ solutions described here will likely be replaced by freeware or proprietary software. Also look for real-time high-quality BOS imaging and perhaps even a BOS smartphone app.

In terms of equipment, the cost of high-speed digital video needs to come down, as it is now unaffordable for many potential users. As well as lower cost, larger memory buffers and higher data transfer rates from image-plane to memory will make these cameras more important for industrial as well as scientific applications. A compact digital streak camera in the megahertz range and above would be a great addition to current commercial instruments, and it has already been done in prototype [150]. 3D printing of custom optical mounts and components will soon be commonplace for the do-it-yourselfer. Whether or not there will be more commercial schlieren and shadowgraph instruments is not clear.

Acknowledgments

References

[1] Settles G S 2001 *Schlieren and Shadowgraph Techniques: Visualizing Phenomena in Transparent Media* (Berlin: Springer)

[2] Krehl P and Engemann S 1995 August Toepler—the first who visualized shock waves *Shock Waves* **5** 1–18

[3] Goodman J W 2004 *Introduction to Fourier Optics* 3rd edn (Englewood, CO: Roberts & Co.)

[4] Schardin H 1942 Die Schlierenverfahren und ihre Anwendungen *Ergebnisse der Exakten Naturwissenschaften* **20** 303–439

[5] Weinstein L M 1993 Large-field high-brightness focusing schlieren system *AIAA J.* **31** 1250–5

[6] Tropea C, Yarin A L and Foss J F 2007 *Springer Handbook of Experimental Fluid Dynamics* (Heidelberg: Springer)

[7] PBS Documentary Film 2012 *Side by Side: The Science, Art and Impact of Digital Cinema* directed by C Kenneally (Los Angeles: Company Films LLC) sidebysidethemovie.com

[8] Hooke R 1665 *Micrographia* (London: J. Martyn and J. Allestry)

[9] Versluis M 2013 High-speed imaging in fluids *Exp. Fluids* **54** 1458

[10] Kleine H 2010 Filming the invisible—time-resolved visualization of compressible flows *Eur. Phys. J. Spec. Top.* **182** 3–34

[11] Kleine H, Le C V, Takehara K and Etoh T G 2010 Time-resolved visualization of shock-vortex systems emitted from an open shock tube *J. Vis.* **13** 33–40

[12] Cranz C and Schardin H 1929 Kinematographie auf ruhendem film und mit extrem hoher Bildfrequenz *Z. Phys.* **56** 147–83

[13] Greenberg P S, Klimek R B and Buchele D R 1995 Quantitative rainbow schlieren deflectometry *Appl. Opt.* **34** 3810–3

[14] Yam F and Hassan Z 2005 Innovative advances in LED technology *Microelectron. J.* **36** 129–37

[15] Albeanu D F, Soucy E, Sato T F, Meister M and Murthy V N 2008 LED Arrays as cost effective and efficient light sources for widefield microscopy *PLoS One* **3** e2146

[16] Bui D A and Hauser P C 2015 Analytical devices based on light-emitting diodes—a review of the state-of-the-art *Anal. Chim. Acta* **853** 46–58

[17] Willert C E, Stasicki B, Klinner J and Moessner S 2010 Pulsed operation of high-power light emitting diodes for imaging flow velocimetry *Meas. Sci. Technol.* **21** 075402

[18] Willert C E, Mitchell D M and Soria J 2012 An assessment of high-power light-emitting diodes for high frame rate schlieren imaging *Exp. Fluids* **53** 413–21

[19] Wilson S, Gustafson G, Lincoln D, Murari K and Johansen C 2015 Performance evaluation of an overdriven LED for high-speed schlieren imaging *J. Vis.* **18** 35–45

[20] Fuller P W W 1999 The use of spark photography in scientific research *Shock Waves* **9** 353–65

[21] Jonassen D R, Settles G S and Tronosky M D 2006 Schlieren 'PIV' for turbulent flows *Opt. Lasers Eng.* **44** 190–207

[22] Dalziel S B, Hughes G O and Sutherland B R 1998 Synthetic schlieren *Proc. 8th Int. Symp. on Flow Visualization* (*Sorrento, Italy*, *1–4 September 1998*) paper 62

[23] Meier G E A 1999 Hintergrund Schlierenmessverfahren *Deutsche Patentanmeldung* DE 199 42 856 A1

[24] Raffel M 2015 Background-oriented schlieren (BOS) techniques *Exp. Fluids* **56** 60

[25] Sutherland B R, Dalziel S B, Hughes G O and Linden P F 1999 Visualization and measurement of internal waves by 'synthetic schlieren' part 1, vertically oscillating cylinder *J. Fluid Mech.* **390** 93–126

[26] Richard H and Raffel M 2001 Principle and applications of the background oriented schlieren (BOS) method *Meas. Sci. Technol.* **12** 1576–85

[27] Dalziel S B, Hughes G O and Sutherland B R 2000 Whole-field density measurements by 'synthetic schlieren' *Exp. Fluids* **28** 322–35

[28] Meier G E A 2002 Computerized background-oriented schlieren *Exp. Fluids* **33** 181–7

[29] Elsinga G E, Van Oudheusden B W, Scarano F and Watt D W 2004 Assessment and application of quantitative schlieren methods: calibrated color schlieren and background oriented schlieren *Exp. Fluids* **36** 309–25

[30] Venkatakrishnan L and Meier G E A 2004 Density measurements using background oriented schlieren technique *Exp. Fluids* **37** 237–47

[31] Kindler K, Goldhahn E, Leopold F and Raffel M 2007 Recent developments in background oriented Schlieren methods for rotor blade tip vortex measurements *Exp. Fluids* **43** 233–40

[32] Goldhahn E and Seume J 2007 The background oriented schlieren technique: sensitivity, accuracy, resolution and application to a three-dimensional density field *Exp. Fluids* **43** 241–9

[33] Atcheson B, Heidrich W and Ihrke I 2009 An evaluation of optical flow algorithms for background oriented schlieren imaging *Exp. Fluids* **46** 467–76

[34] Hargather M J and Settles G S 2010 Natural-background-oriented schlieren imaging *Exp. Fluids* **48** 59–68

[35] Hargather M J and Settles G S 2012 A comparison of three quantitative schlieren techniques *Opt. Lasers Eng.* **50** 8–17

[36] Sourgen F, Leopold F and Klatt D 2012 Reconstruction of the density field using the colored background oriented schlieren technique (CBOS) *Opt. Lasers Eng.* **50** 29–38

[37] Bichal A and Thurow B S 2014 On the application of background oriented schlieren for wavefront sensing *Meas. Sci. Technol.* **25** 015001

[38] Heineck J T, Banks D, Schairer E T, Haering E A and Bean P 2016 Background oriented schlieren (BOS) of a supersonic aircraft in flight *AIAA J.* submitted (AIAA Paper 2016-3356) (doi:10.2514/6.2016-3356)

[39] Hill M A and Haering E A Jr 2017 Ground to air flow visualization using solar calcium-K line background oriented schlieren *Exp. Fluids* **58**

[40] Bauknecht A, Ewers B, Wolf C, Leopold F, Yin J P and Raffel M 2015 Three-dimensional reconstruction of helicopter blade-tip vortices using a multi-camera BOS system *Exp. Fluids* **56** 1866

[41] Raffel M, Heineck J T, Schairer E, Leopold F and Kindler K 2014 Background-oriented schlieren imaging for full-scale and in-flight testing *J. Am. Helicopter Soc.* **59** 012002

[42] Sommersel O K, Bjerketvedt D, Christensen S O, Krest O and Vaagsaether K 2008 Application of background oriented schlieren for quantitative measurements of shock waves from explosions *Shock Waves* **18** 291–7

[43] Hargather M J 2013 Background-oriented schlieren diagnostics for large-scale explosive testing *Shock Waves* **23** 529–36

[44] Mizukaki T, Wakabayashi K, Matsumura T and Nakayama K 2014 Background-oriented schlieren with natural background for quantitative visualization of open-air explosions *Shock Waves* **24** 69–78

[45] Reinholtz C K, Heltsley F L and Scott K E 2010 Plume visualization of Orion Launch Abort Vehicle jettison motors using background-oriented schlieren *USAF Arnold Engineering Development Center Report* AEDC-TR-09-T-13

[46] Bathel B F, Borg S, Jones S B, Overmeyer A, Walker E, Goad W, Clem M M, Schairer E and Mizukaki T 2015 Development of background-oriented schlieren for NASA Langley Research Center ground test facilities AIAA Paper 2015-1691 (DOI: 10.2514/6.2015-1691)

[47] LaVision 2015 Background Oriented Schlieren imaging of a thermal flow https://youtu.be/mgD6Uag14EA

[48] Perciante C D and Ferrari J A 2000 Visualization of two-dimensional phase gradients by subtraction of a reference periodic pattern *Appl. Opt.* **39** 2081–3

[49] Ambrosini D, Guattari G, Sapia C and Schirripa Spagnolo G 2000 Flow visualization via fringe projection *Proc. 9th Int. Symp. Flow Visualization* paper 117

[50] Bühlmann P, Meier A H, Ehrensperger M and Rösgen T 2014 Laser speckle based background oriented schlieren measurements in a fire backlayering front *Proc. 17th Int. Symp. Apps. Laser Techn. Fluid Mech.*

[51] Settles G S 2016 Background-Oriented Schlieren (BOS) of oscillating Bunsen burner flame https://youtu.be/8wUn_UvwfgI

[52] Dalziel S B 2012 personal communication

[53] Hargather M J and Settles G S 2011 Background-oriented schlieren visualization of heating and ventilation flows: HVAC-BOS *HVAC&R Res.* **17** 771–80

[54] Vinnichenko N A, Uvarov A V and Plaksina Y Y 2012 Accuracy of background-oriented schlieren for different background patterns and means of refractive index reconstruction *Proc. 15th Int. Symp. Flow Visualization* paper 86

[55] Bauknecht A, Merz C B, Raffel M, Landolt A and Meier A H 2014 Blade-tip vortex detection in maneuvering flight using the background-oriented schlieren technique *J. Aircr.* **51** 2005–14

[56] Rinkevichius B S, Skornyakova N M, Mikhaleva E M, Mikhalev A S, Poroykov A Y and Udalov A V 2013 Investigation of background pattern for the outdoor application of the BOS method *Advanced In-Flight Measurement Techniques* ed F Boden (Berlin: Springer) pp 305–20 ch 18

[57] Mier F A and Hargather M J 2016 Color gradient background-oriented schlieren imaging *Exp. Fluids* **57** 95

[58] Meier A H and Rösgen T 2013 Improved background oriented schlieren imaging using laser speckle illumination *Exp. Fluids* **54** 1549

[59] Briers J D 1993 Holographic, speckle and moiré techniques in optical metrology *Prog. Quantum Electron.* **17** 167–233

[60] Gojani A B, Kamishi B and Obayashi S 2013 Measurement sensitivity and resolution for background oriented schlieren during image recording *J. Vis.* **16** 201–7

[61] Pan B, Qian K M, Xie H M and Asundi A 2009 Two-dimensional digital image correlation for in-plane displacement and strain measurement: a review *Meas. Sci. Technol.* **20** 17

[62] Smith N T, Heineck J T and Schairer E T 2017 Optical flow for flight and wind tunnel background oriented schlieren imaging. *55th AIAA Aerospace Sciences Meeting*, AIAA 2017-0472 (DOI: 10.2514/6.2017-0472)

[63] Letelier J A, Herrera P, Mujica N and Ortega J H 2016 Enhancement of synthetic schlieren image resolution using total variation optical flow: application to thermal experiments in a Hele–Shaw cell *Exp. Fluids* **57** 18

[64] Liu T S, Merat A, Makhmalbaf M H M, Fajardo C and Merati P 2015 Comparison between optical flow and cross-correlation methods for extraction of velocity fields from particle images *Exp. Fluids* **56** 166

[65] Collins T J 2007 ImageJ for microscopy *Biotechniques* **43** 25–30

[66] Thompson P A 1972 *Compressible-Fluid Dynamics* (New York: McGraw-Hill) ch 8

[67] Domens P, Dupuy J, Gibert A, Diaz R, Hutzler B, Riu J P and Ruehling F 1988 Large air-gap discharge and schlieren techniques *J. Phys. D: Appl. Phys.* **21** 1613–23

[68] Katayama A S 1994 Visualization techniques for temporally acquired sequences of images *US Patent* 5294978

[69] Katayama A S 1999 Streak visualization: a new analysis tool for the evaluation of video sequences *Proc. SPIE* **3642** 80–91

[70] Biss M M and Settles G S 2010 On the use of composite charges to determine insensitive explosive material properties at the laboratory scale *Propellants Explos. Pyrotech.* **35** 452–60

[71] Biss M M and McNesby K L 2014 Optically measured explosive impulse *Exp. Fluids* **55** 174

[72] Giannuzzi P M, Hargather M J and Doig G C 2016 Explosive-driven shock wave and vortex ring interaction with a propane flame *Shock Waves* **26** 851

[73] Svingala F R, Hargather M J and Settles G S 2012 Optical techniques for measuring the shock Hugoniot using ballistic projectile and high-explosive shock initiation *Int. J. Impact Eng.* **50** 76–82

[74] Settles G S, Young R M, Svingala F R and Glusman J F 2015 Optical shock Hugoniot measurements of transparent and translucent polymers *Elastomeric Polymers with High Rate Sensitivity* ed R G S Barsoum (New York: Elsevier) ch 3.5

[75] Handa T, Miyachi H, Kakuno H and Ozaki T 2012 Generation and propagation of pressure waves in supersonic deep-cavity flows *Exp. Fluids* **53** 1855–66

[76] Hargather M J, Settles G S and Gogineni S 2013 Optical diagnostics for characterizing a transitional shear layer over a supersonic cavity *AIAA J* **51** 2977–82

[77] Sridhar V, Kleine H and Gai S L 2015 Visualization of wave propagation within a supersonic two-dimensional cavity by digital streak schlieren *Exp. Fluids* **56** 152

[78] Kleine H, Dewey J M, Ohashi K, Mizukaki T and Takayama K 2003 Studies of the TNT equivalence of silver azide charges *Shock Waves* **13** 123–38

[79] Hargather M J and Settles G S 2007 Optical measurement and scaling of blasts from gram-range explosive charges *Shock Waves* **17** 215–23

[80] Timmerman B H, Skeen A J, Bryanston-Cross P J, Tucker P G, Jefferson-Loveday R J, Paduano J and Guenette G R 2008 High-speed digital visualization and high-frequency automated shock tracking in supersonic flows *Opt. Eng.* **47** 103201

[81] Weinstein L M 2010 Review and update of lens and grid schlieren and motion camera schlieren *Eur. Phys. J. Spec. Top.* **182** 65–95

[82] Settles G S 2016 Slit-scan schlieren imaging with the iPhone *Proc. 17th Int. Symp. on Flow Visualization* ed K D Kihm paper 095

[83] Haering E A Jr, Bean P S, Jones T P, Buckner B D and L'Esperance D 2016 Imaging shockwaves and vortices on full-scale aircraft using schlieren photography with the sun's limb from the ground and from an aircraft *Proc. 17th Int. Symp. Flow Visualization* ed K D Kihm paper 010

[84] Townend H C H 1936 A method of airflow cinematography capable of quantitative analysis *J. Aero. Sci.* **3** 343–52

[85] Hargather M J, Lawson M J, Settles G S and Weinstein L M 2011 Seedless velocimetry measurements by schlieren image velocimetry *AIAA J.* **49** 611–20

[86] Papamoschou D I 1989 A two-spark schlieren system for very-high velocity measurement *Exp. Fluids* **7** 354–6

[87] Fu S and Wu Y J 2001 Detection of velocity distribution of a flow field using sequences of schlieren images *Opt. Eng.* **40** 1661–6

[88] Pope S B 2000 *Turbulent Flows* (Cambridge: Cambridge University Press)

[89] Bracewell R 2003 *Fourier Analysis and Imaging* (New York: Kluwer Academic)

[90] Mauger C, Mees L, Michard M and Lance M 2014 Velocity measurements based on shadowgraph-like image correlations in a cavitating micro-channel flow *Int. J. Multiph. Flow* **58** 301–12

[91] Sun C L and Huang C Y 2014 Microscale schlieren visualization of near-bubble mass transport during boiling of 2-propanol/water mixtures in a square capillary *Exp. Fluids* **55** 1778

[92] Raffel M, Hernandez-Rivera R, Heine B, Schröder A and Mulleners K 2011 Density tagging velocimetry *Exp. Fluids* **51** 573–8

[93] Garg S and Settles G S 1998 Measurements of a supersonic turbulent boundary layer by focusing schlieren deflectometry *Exp. Fluids* **25** 254–64

[94] Garg S and Cattafesta L N III 2001 Quantitative schlieren measurements of coherent structures in a cavity shear layer *Exp. Fluids* **30** 123–34

[95] Doty M J and McLaughlin D K 2005 Space-time correlation measurements of high-speed axisymmetric jets using optical deflectometry *Exp. Fluids* **38** 415–25

[96] Chan S H, Vo D T and Nguyen T Q 2010 Subpixel motion estimation without interpolation *Proc. 2010 IEEE Int. Conf. Acoustics, Speech, Signal Processing* pp 722–5

[97] Thurow B S, Jiang N I B, Kim J H, Lempert W and Samimy M 2008 Issues with measurements of the convective velocity of large-scale structures in the compressible shear layer of a free jet *Phys. Fluids* **20** 066101

[98] Tobin J D and Hargather M J 2016 Quantitative schlieren measurement of explosively-driven shock wave density, temperature, and pressure profiles *Propellants Explos. Pyrotech.* **41** 1050–9

[99] Howes W L 1983 Rainbow schlieren NASA Technical Paper TP-2166 (Cleveland OH: NASA Glenn Research Center)

[100] Howes W L 1984 Rainbow schlieren and its applications *Appl. Opt.* **23** 2449–60

[101] Agrawal A K, Butuk N K and Gollahalli S R 1998 Three-dimensional rainbow schlieren tomography of a temperature field in gas flows *Appl. Opt.* **37** 479–85

[102] Kolhe P S and Agrawal A K 2009 Density measurements in a supersonic microjet using miniature rainbow schlieren deflectometry *AIAA J.* **47** 830–8

[103] Sznitman J and Rösgen T 2006 Whole-field density visualization and Abel reconstruction of axisymmetric vortex rings *J. Flow Vis. Image Proc.* **13** 343–58

[104] Venkatakrishnan L and Suriyanarayanan P 2009 Density field of supersonic separated flow past an afterbody nozzle using tomographic reconstruction of BOS data *Exp. Fluids* **47** 463–73

[105] Ishino Y, Hayashi N, Bt Abd Razak I F, Kato T, Kurimoto Y and Saiki Y 2016 3D-CT (computer tomography) measurement of an instantaneous density distribution of turbulent flames with a multi-directional quantitative schlieren camera (reconstructions of high-speed premixed burner flames with different flow velocities) *Flow Turbul. Combust.* **96** 819–35

[106] Wikipedia 2016 List of ray tracing software https://en.wikipedia.org/wiki/List_of_ray_tracing_software

[107] Texereau J 1963 *How to Make a Telescope* (Garden City, NY: Anchor Books)

[108] Kikuchi D and Sun M 2009 Numerical analysis of optical systems for compressible flow visualization *Computational Fluid Dynamics 2008* ed H Choi *et al* (Berlin: Springer) pp 801–4

[109] Kirmse T, Agocs J, Schröder A, Schramm J M, Karl S and Hannemann K 2011 Application of particle image velocimetry and the background-oriented schlieren technique in the high-enthalpy shock tunnel Göttingen *Shock Waves* **21** 233–41

[110] Kaiser S A, Salazar V M and Hoops A A 2013 Schlieren measurements in the round cylinder of an optically accessible internal combustion engine *Appl. Opt.* **52** 3433–43

[111] Yates L A 1992 Interferograms, schlieren, and shadowgraphs constructed from real- and ideal-gas, two- and three-dimensional computed flowfields NASA-CR-190054 Contractor Report by Eloret Corp., Mountain View CA (https://ntrs.nasa.gov/archive/nasa/casi.ntrs.nasa.gov/19920012113.pdf)

[112] Yates L A 1993 Images constructed from computed flowfields *AIAA J.* **31** 1877–84

[113] Shenoy A K, Agrawal A K and Gollahalli S R 1998 Quantitative evaluation of flow computations by rainbow schlieren deflectometry *AIAA J.* **36** 1953–60

[114] Brassington G B, Patterson J C and Lee M 2002 A new algorithm for analyzing shadowgraph images *J. Flow Vis. Image Proc.* **9** 25–51

[115] Jiang Z L 2003 Wave dynamic processes induced by a supersonic projectile discharging from a shock tube *Phys. Fluids* **15** 1665–75

[116] Terashima H and Tryggvason G 2009 A front-tracking/ghost-fluid method for fluid interfaces in compressible flows *J. Comput. Phys.* **228** 4012–37

[117] Naughton J W, Venkatapathy E and Fletcher D G 1995 Combined computational/experimental flow field imaging for efficient testing *Flow Visualization VII* ed J P Crowder (New York: Begell House) pp 832–7

[118] Martín M P, Taylor E M, Wu M and Weirs V G 2006 A bandwidth-optimized WENO scheme for the effective direct numerical simulation of compressible turbulence *J. Comput. Phys.* **220** 270–89

[119] Brownlee C, Pegoraro V, Shankar S, McCormick P S and Hansen C D 2011 Physically-based interactive flow visualization based on schlieren and interferometry experimental techniques *IEEE Trans. Vis. Comput. Graph.* **17** 1574–86

[120] Samtaney R and Zabusky N J 2000 Visualization, feature extraction and quantification of numerical visualizations of high gradient compressible flows *Flow Visualization Techniques and Examples* ed A J Smits and T T Lim (London: Imperial College Press) pp 317–44

[121] Liang S M and Chen H 2003 Flow visualization of numerically simulated blast waves discharging from open-ended duct *AIAA J.* **41** 2420–8

[122] Hadjadj A and Kudryavtsev A 2005 Computation and flow visualization in high-speed aerodynamics *J. Turbul.* **6** 1–25

[123] Quirk J J 1994 A contribution to the great Riemann solver debate *Int. J. Num. Methods Fluids* **18** 555–74

[124] Dauptain A, Cuenot B and Gicquel L Y M 2010 Large eddy simulation of stable supersonic jet impinging on flat plate *AIAA J.* **48** 2325–38

[125] Edgerton H E 1970 *Electronic Flash, Strobe* (Cambridge, MA: MIT Press)

[126] Edgerton H E 1958 Shockwave photography of large subjects in daylight *Rev. Sci. Instrum.* **29** 171–2

[127] Biele J K 2003 Point-source spark shadowgraphy at the historic birthplace of supersonic transportation—a historical note *Shock Waves* **13** 167–77

[128] Parthasarathy S P, Cho Y I and Back L H 1987 Wide-field shadowgraphy of tip vortices from a helicopter rotor *AIAA J.* **25** 64–70

[129] Leishman J G and Bagai A 1996 Challenges in understanding the vortex dynamics of helicopter rotor wakes *AIAA J.* **36** 1130–40

[130] Hargather M J and Settles G S 2009 Retroreflective shadowgraph technique for large-scale flow visualization *Appl. Opt.* **48** 4449–57

[131] Settles G S 2006 High-speed imaging of shock waves, explosions and gunshots *Am. Sci.* **94** 22–31

[132] Taylor M C, Laber T L, Epstein B P, Zamzow D S and Baldwin D P 2011 The effect of firearm muzzle gases on the backspatter of blood *Int. J. Leg. Med.* **125** 617–28

[133] Dennis K, Maley L, Liang Z and Radulescu M I 2014 Implementation of large scale shadowgraphy in hydrogen explosion phenomena *Int. J. Hydrog. Energy* **39** 11346–53

[134] McNesby K L, Homan B E, Benjamin R A, Boyle V M, Densmore J M and Biss M M 2016 Invited Article: Quantitative imaging of explosions with high-speed cameras *Rev. Sci. Instrum.* **87** 051301

[135] Slangen P R, Lauret P, Heymes F, Aprin L and Lecysyn N 2016 High-speed imaging optical techniques for shockwave and droplets atomization analysis *Opt. Eng.* **55** 121706

[136] Talley M A, Jones S B and Goodman W L 2000 Development of a large field of view shadowgraph system for a 16 ft. transonic wind tunnel NASA Technical Memorandum TM-2000-210311 (https://ntrs.nasa.gov/archive/nasa/casi.ntrs.nasa.gov/20000108883.pdf)

[137] Nelson C T 2004 Some results from a simple shadowgraph system in the Boeing Transonic Wind Tunnel *Proc. 11th Int. Symp. Flow Visualization* ed T J Mueller and I Grant paper 47

[138] ASTM 2005 Standard test method for capture and containment performance of commercial kitchen exhaust ventilation systems Standard F 1704-05 (Conshohocken PA: ASTM International)

[139] Sinur R R, Wellnitz B R, Perkins J F and Montag S 2016 Downdraft system *US Patent* 9297540B2 assignee Broan-Nutone LLC

[140] Bestrangehoods.com/cattura 2016 Shadowgraph imaging proves BEST Cattura Downdraft has superior capture ability https://youtu.be/pNVRQzWGvNk

[141] Buckner B D and L'Esperance D 2013 Digital synchroballistic schlieren camera for high-speed photography of bullets and rocket sleds *Opt. Eng.* **52** 083105

[142] Buckner B D and L'Esperance D 2016 Digital schlieren imaging *US Patent* 9232117 B2

[143] Trolinger J D, Buckner B D and L'Esperance D 2015 Background-oriented schlieren for the study of large flow fields *Proc. SPIE* **9576** 95760E

[144] Wetzstein G, Raskar R and Heidrich W 2011 Hand-held schlieren photography with light field probes *Proc. IEEE Int. Conf. on Computational Photography* pp 1–8

[145] Wetzstein G, Heidrich W and Raskar R 2014 Computational schlieren photography with light field probes *Int. J. Comput. Vis.* **110** 113–27

[146] Klemkowsky J, Thurow B and Mejia R 2016 3D visualization of compressible flow using a plenoptic camera and background oriented schlieren AIAA Paper 2016-1047 DOI: 10.2514/6.2016-1047

[147] Glaeser R M 2013 Invited review article: methods for imaging weak-phase objects in electron microscopy *Rev. Sci. Instrum.* **84** 111101

[148] Nagayama K 2014 Biological applications of phase-contrast electron microscopy *Electron Microscopy: Methods and Protocols* ed J Kuo (New York: Springer) pp 385–99 ch 18

[149] Biss M M, Settles G S and Sanderson S R 2008
    Differential schlieren-interferometry with a
    simple adjustable Wollaston-like prism *Appl. Opt.*
    47 328–35

[150] Uhring W, Le Normand J P, Zint V and Zlatanski M
    2010 Integrated streak camera in standard (Bi)CMOS
    technology *Proc. SPIE* **7719** 77190V

[151] Settles G S 2010 Important developments in schlieren
    and shadowgraph visualization during the last decade
    Proc. 14th Int. Symp. Flow Visualization ed K C Kim
    paper 267

[152] Hargather M J and Settles G S 2010 Recent developments in
    schlieren and shadowgraphy AIAA Paper 2010-4206 DOI:
    10.2514/6.2010-4206